Applied Water Science (2024) 14:83
https://doi.org/10.1007/s13201-024-02125-2

ORIGINAL ARTICLE

Integrated stratigraphical, hydrogeochemical, and geophysical studies to characterize the shallow groundwater aquifers in Wadi Araba area, western Gulf of Suez, Egypt

Zenhom E. Salem[1] · Maha Abdelazeem[2] · Mohamed Mostafa Khalifa[2] · Mohamed Sobhy Fathy[1]

Received: 23 November 2022 / Accepted: 1 February 2024

Abstract

The construction of the New Galala City besides great mining (e.g., konoozmisr) and Seawater Reverse Osmosis Desalination Plant projects in the semiarid Gulf of Suez region of Egypt increases the demand for groundwater resources. So, the current research provides integrated stratigraphical, hydrogeochemical, and geophysical studies to investigate the shallow groundwater aquifers in Wadi Araba area on the western side of the Gulf of Suez. The stratigraphic column starts with pre-Cambrian basement rocks which are non-conformably overlain by sedimentary succession of Phanerozoic Erathem. A detailed land magnetic profile has been conducted and processed to estimate the aquifer's geometrical parameters. This includes the subsurface spatial extension and thickness to delineate the prevailed subsurface structures in the study area. Lithostratigraphically, these aquifers are represented by the Paleozoic- lower Cretaceous siliciclastic-dominated sediments of the Nubia Group and fractured carbonate-dominated facies of the upper Cretaceous Galala Formation. Lithological characters, sedimentary facies (fluvial to shallow and open marine), microfacies types, and diagenesis processes (e.g., compaction, cementation, dissolution, and fracturing) are the main factors that affect the quality of the shallow aquifers in the study area. The main microfacies of the studied aquifers are quartz arenite, subarkose, sublitharenite, mudstone/wackestone, and packstone/grainstone. These facies are characterized by different primary and secondary porosities. According to the water sampling standard methods, nineteen groundwater samples were collected from the available hand-dug wells and springs from the Nubian sandstone aquifer and the Upper Cretaceous aquifer, respectively. Inductively coupled plasma–mass spectrometry (ICP–MS), titration, spectrophotometer and a flame photometer were used to obtain a complete chemical analysis. The results of hydrochemical analyses indicated that total dissolved solids (TDS) and concentrations of major ions as well in the lower Cretaceous aquifer increase toward the Gulf of Suez and in general higher than that of springs of the Upper Cretaceous Aquifer. The predominant factors influencing groundwater chemistry include seawater intrusion, evaporation, mineral alteration, dissolution of fossils, and ion exchange. Groundwater in the study area is unsuitable for drinking except in one sample and moderately suitable for irrigation with caution for higher salinity in samples located near the Gulf of Suez.

Keywords Wadi Araba · Nubian sandstone aquifer · Carbonate sediments · Aquifer quality · Magnetic tomography · Gulf of Suez

✉ Maha Abdelazeem
maazeem03@nriag.sci.eg

Zenhom E. Salem
zenhomsalem@yahoo.com

Mohamed Mostafa Khalifa
moh.moustafa92@gmail.com

Mohamed Sobhy Fathy
msfathy@science.tanta.edu.eg

[1] Geology Department, Faculty of Science, Tanta University, Tanta, Egypt

[2] Geomagnetism and Geoelectricity Department, National Research Institute of Astronomy and Geophysics, Helwan, Cairo, Egypt

Published online: 21 March 2024

Introduction

Egypt's current principal challenge is the dire need for better development and management of the country's finite water, land, and energy resources to meet the country's population growth needs (Ashour et al. 2009). Groundwater represents the main source of freshwater supply for the local inhabitants. As tourism activities, quarrying, and the population of the area increase, spatial attention should be focused on the future development of the water supplies of Wadi Araba, west of the Gulf. In this respect, ambitious plans for groundwater exploration and evaluation are required (Aggour 1990). Nowadays, the demand for groundwater increased in the studied area because of the construction of the New Galal City close to Wadi Araba.

The area of study is located on the western side of the Gulf of Suez. It is bounded by latitudes 28° 30` and 29° 30` N and longitudes 31° 45` and 32° 45` E (Fig. 1) and extends in an E–W direction between Northern Galala and Southern Galala plateaus with a total length and area of about 40 km and 1100 Km^2, respectively. The geological map of the area under study is shown (Fig. 2), which is modified after Conoco (1987). Since Schweinfurth (1885) recorded the Paleozoic fossils in Wadi Araba, the area attracted many geologists to investigate the stratigraphical and structural settings of the area. Most of the rock units of the Paleozoic–Mesozoic sequences of the studied area (e.g., Rod El Hamal, Qiseib, and Malha formations) were introduced by Abdallah and El Adendani (1963) and Abdallah et al. (1965). A revision of the lithostratigraphic classification of the Permo-Carboniferous outcrops of the Gulf of Suez region was carried out by Kora and Mansour (1992). Bandel and Kuss (1987) delineated the depositional environment of Palaeozoic–Eocene sediments at the Northern and Southern Galala plateau, which ranged from fluvial to open marine environments. Petrophysically, Nabawy et al. (2020) noted that the porosity and

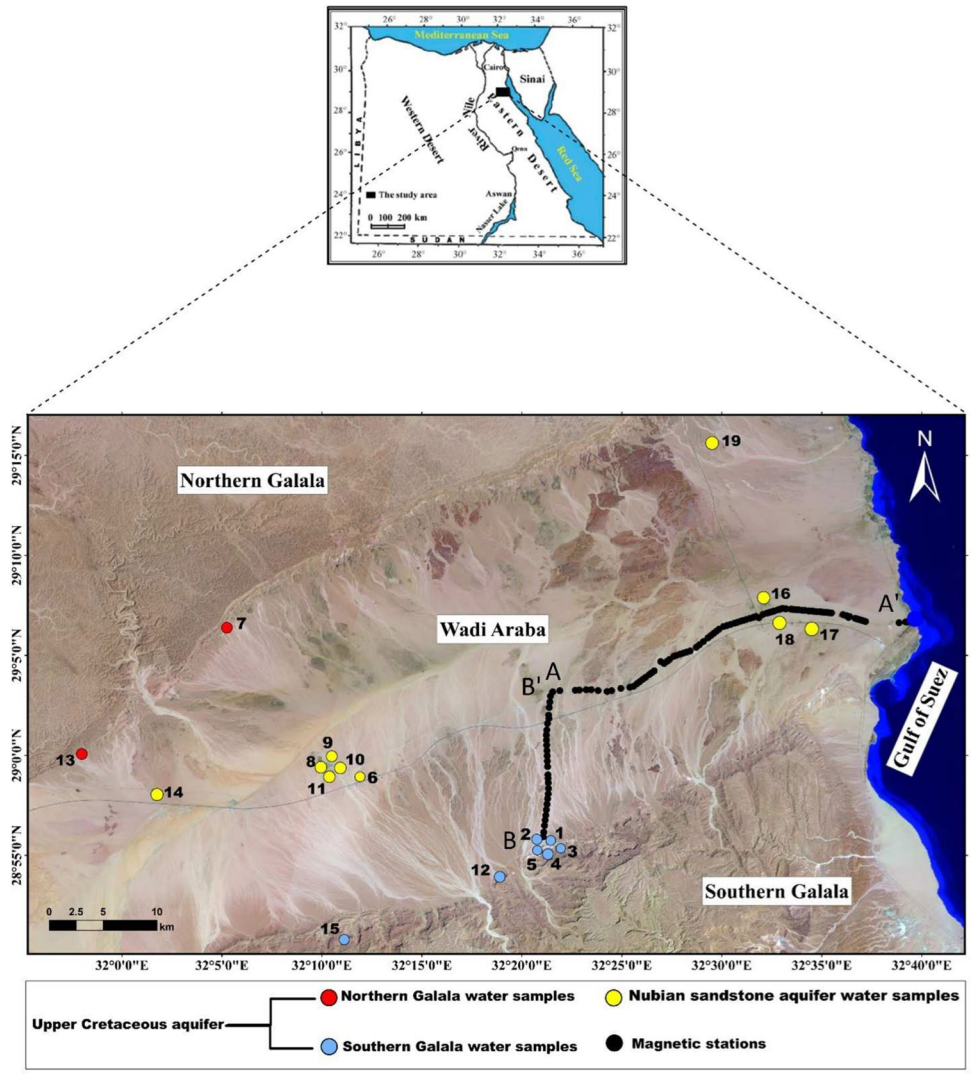

Fig. 1 Location map of the study area, west of the Gulf of Suez, Egypt with position of the studied boreholes, collected rock samples and land magnetic measurements on the Landsat image of Wadi Araba, west Gulf of Suez, Egypt

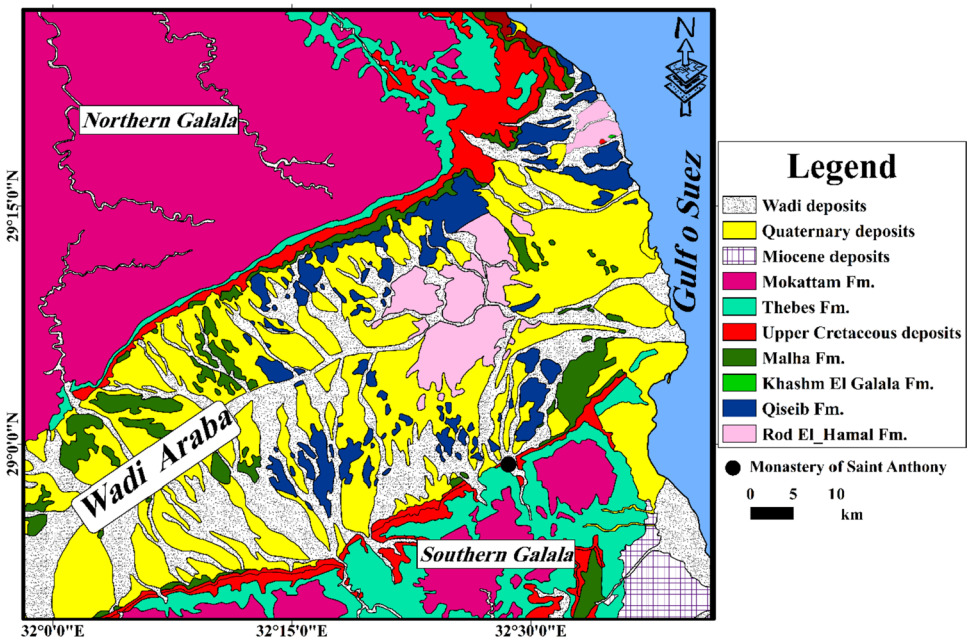

Fig. 2 Geological map of the studied Wadi Araba area (*modified after* Conoco 1987)

permeability of the Nubian microfacies of quartz arenite, sublitharenite and arkose are good to excellent, whereas the ferruginous subarkose to greywacke is characterized by relatively less petrophysical potential than the others.

Two structural phases were detected by Moustafa and Khalil (1994) in the Gulf of Suez region. In the Late Cretaceous phase of deformation, folds with NE–SW oriented axes were formed in northern Egypt as a result of convergence between Africa and Eurasia and the closure of the Neotethys. In the second early Miocene phase, deformation NW-oriented normal faults were formed as a result of the opening of the Suez Rift. The tertiary carbonate platform in the studied area formed as a result of the initial topography that was controlled by the tectonic uplift of the Northern Galala/Wadi Araba Syrian Arc structure (Scheibner et al. 2001).

Aggour (1990) elucidated the hydrogeologic framework of Wadi Araba. He classified Wadi Araba as a high Wadi according to its relative groundwater possibility. Rocks belonging to Carboniferous and Lower Cretaceous sandstone (Nubian aquifer) represent the main source of water in the Wadi Araba depression. The water is tapped from springs, shallow wells, and occasionally deep wells. The quaternary alluvium deposits constitute an insignificant water-bearing horizon. Gomaa and Aggour (1999) studied the hydrogeological and hydrogeochemical conditions of carbonate aquifers in the Gulf of Suez region. They considered that the carbonate rocks represent productive aquifers on both sides of the Gulf of Suez. These rocks constitute extensive watershed areas, e.g., Northern Galala, Southern Galala, and Abu Sha'r plateau on the western side. Some recommendations were proposed in this study for the development of groundwater resources. Hand-dug wells are suggested along the scraps of the plateaus at the favorable sites and more attention should be focused on the utilization of the flowing water such as the construction of surface reservoirs to control the discharge and use. Younis et al. (2019) used VES/TEM techniques at the North Galala plateau to assess the present situation of groundwater in the Quaternary and Pliocene aquifers. They found groundwater in the shallow aquifer might be of good quality than the water in the deep aquifer. They also found the most appropriate areas for burrowing new water wells.

On the other hand, the magnetic method is a geophysical technique that proved its efficiency when applied to hydrogeological investigations. Of all geophysical techniques, the magnetic method is the most versatile since it may be used for both shallow and deep research (Dobrin and Savit 1988). Additionally, it is affordable and includes both local and regional investigations. The magnetic method has primarily been used for regional surveys in hydrocarbon exploration (Abdelazeem et al. 2020, 2021; De Smet et al. 2020; Abdelrahman et al. 2019; Gobashy and Al-Garni 2008; Al Garni et al. 2006); engineering geophysics (Araffa et al. 2021; Azeem et al 2014); groundwater exploration (Gobashy et al. 2021b); mineral exploration (Gobashy et al. 2022, 2021a; El-Sawy et al. 2018; Abdelrahman et al. 2019); and mapping geological structures and igneous intrusions (Al Garni et al. 2012; Wang et al. 2017); in addition, estimating sedimentary basin thickness and identifying groundwater contamination (Nazih et al. 2022; Rehman et al. 2019) and geologic hazard and risk assessments (Fergany et al. 2014; Al Garni and Gobashy 2010) are examples of a such wide range of applications.

Based on the magnetic method, Abdelazeem et al. (2019) have delineated the main structures in this area as NW–SE, and E–W trends, with minor trends as the N–S, NE, ENE, WNW, NNW, NNE, and ENE, and noted that the carbonate rocks suffered from various diagenetic processes for a long time and have different caves, joints, sinkholes, and karst surfaces.

With the remarkable variations in the Wadi Araba vertical and lateral facies, the goal of this study is to explore and identify qualitatively the shallow groundwater aquifer from the detailed integrated petrographic, stratigraphic, geochemical, and geophysical point of view. The study aims to support groundwater sustainability and conservation. To identify the subsurface structure geometries, magnetic tomography is essentially used. The findings should help control the area's subterranean water resources to prevent the region's groundwater levels and quality from declining and facilitate upcoming upgrades within the region. The workflow presented helps globally to preserve and develop groundwater resources.

Methodology

Data collection

In the study area, 115 rock samples (WA1 to WA115) have been collected and described from the exposed Carboniferous–Cretaceous successions, and 47 blue-dyed thin sections are investigated and photographed under the polarized microscope for microfacies analysis, diagenesis, and for rock porosity estimation. The classification of Pettijohn et al. (1987) was used to classify the sandstones of the Nubia Group, whereas the classification of Dunham (1962) and Folk (1962) for carbonate rocks is adopted in the present work. Moreover, a total of 112 magnetic stations were measured along geologically selected localities. The measurements were carried out by using an Over-Houser magnetometer (GSM-19 v7.0) with a sensitivity of 0.022 nT@1 Hz. El Misallat station in Fayoum is considered as the base station (used for diurnal correction). Land magnetic data were conducted using GSM-19 v7.0 with the same sensitivity along a selected profile running from west to east as shown in Fig. 1. The total number of stations is 112 measured according to the accessibility of the area. The measurements are carried out on stations marked every 200–500 m, which is suitable to the objective of the study, to explore the aquifer and the effect of the structure on it.

There are no distributed drilled water wells (except one well) in the study area because there are no agriculture, urban or industrial activities. Therefore, the hydrogeochemical study was undertaken by collecting 16 groundwater samples during April from the available dug wells, one borehole, and springs. The dug wells and the drilled well are tapped from the Nubian sandstone aquifer (from the mainstream of Wadi Araba) and the springs are tapped from the Upper Cretaceous limestones (Southern escarp of the Northern Galala and Northern escarp of the Southern Galala plateaus). Samples 17, 18, and 19 chemical analyses were obtained from Ezzeldin (2010) because it was not possible to sample them as the weathering products covered the spring itself. Water was sampled in new—additionally, rinsed—plastic bottles, and chemical analysis were done a few days after sampling.

Hydrogeochemical analyses

Parameters such as pH (Portable Consort pH Meter, Model P 314), electrical conductivity (EC), and TDS (Hach's Portable Conductivity/Total dissolved solids TDS Meter) were measured for the collected samples in the field (Hach 1990). Major and trace ions were analyzed in the central laboratory of the Desert Research Centre (DRC). ICP–MS (inductively coupled plasma–mass spectrometry) which applies to the determination of sub-µg/L concentration of a large number of elements in water samples (Hoaghia et al. 2021) was used for trace elements analyses. Digital Titration method was applied for determining the concentration of CO_3^{2-} and HCO_3^- against a standard sulfuric acid solution, $Ca^{++}$and Mg^{++} using a total hardness test and chloride using a standard solution of mercuric nitrate and diphenylcarbazone reagent powder. SO_4^{2-} concentration was measured by spectrophotometer (Hach's Direct Reading (DR)/2000) precipitation with barium chloride. A flame photometer was used for Na^+ and K^+ determination (Banerjee and Prasad 2020). The obtained hydrochemical analysis has a charge balance error of less than 5%. The sample's locations map is shown in Fig. 1, and the statistical summary of concentration of the measured hydrochemical parameters in the two aquifers are listed in Tables 1 and 2.

Result and discussions

Magnetic data

Land magnetic profile

Regular data reduction is considered including diurnal reduction (subtracting base station readings from the measured field) and denoising filtering (omitting the odd readings). The reduced-to-pole filter is then applied (using ZondGM2D) to overcome the geomagnetic field polarity shift. The resulting RTP data are then interpreted. Euler deconvolution has also been applied (using ZondGM2D) to ensure the expected faults/contacts.

Table 1 Statistical summary of concentration of the measured major ions

	Aquifers	pH	EC	TDS	TH	CATIONS				ANIONS			
			µS/cm			mg/l							
						K^+	Na^+	Mg^{++}	Ca^{++}	Cl^-	$SO4^{--}$	$HCO3^-$	$CO3^{--}$
MAX	Galala Fm	9	13,646	8734	886	8	2900	144	189	2055	2650	1327	292
MIN		7	1987	951	508	3	180	41	21	397	166	159	0
STDEV		1	3721	2442	133	2	871	34	45	521	788	380	96
Average		8	4021	2336	629	5	609	77	125	755	590	316	36
MAX	Nubia Group	8	38,520	24,770	7064	264	7200	751	2010	13,947	3001	325	26
MIN		5	3266	1745	525	3	420	41	142	590	277	31	0
STDEV		1	13,998	8625	2337	80	2523	249	589	5259	962	87	12
Average		8	14,441	8995	2612	52	2354	274	594	4627	1197	127	11

Table 2 Statistical summary of concentration of the measured trace elements

	Aquifers	Al	Cd	Co	Cr	Cu	Fe	Mn	Mo	Ni	Pb	V	Zn	Si
		mg/l												
Max	Galala Fm	0.779	0.001	0.001	0.000	0.032	0.245	0.084	0.013	0.003	0.215	0.057	0.088	32.646
Min		0.000	0.000	0.000	0.000	0.000	0.000	0.000	0.000	0.000	0.000	0.000	0.000	4.175
STDEV		0.248	0.000	0.000	0.000	0.011	0.085	0.027	0.004	0.001	0.083	0.020	0.031	9.229
Average		0.155	0.000	0.000	0.000	0.004	0.039	0.013	0.004	0.000	0.041	0.011	0.022	8.434
Max	Nubia Group	0.456	0.001	0.003	0.047	0.029	60.350	10.890	0.006	0.013	0.235	0.054	1.337	29.548
Min		0.000	0.000	0.000	0.000	0.000	0.000	0.000	0.000	0.000	0.000	0.000	0.000	0.271
STDEV		0.180	0.000	0.001	0.015	0.011	18.904	3.425	0.002	0.004	0.093	0.022	0.426	10.572
Average		0.192	0.000	0.001	0.005	0.005	7.108	1.337	0.003	0.002	0.062	0.019	0.187	10.271

Quantitative interpretation

Quantitative magnetic interpretation is an essential step for the delineation of subsurface structures and the distribution of rock units. The surface magnetic anomalies have resulted from subsurface variations (either lateral or vertical) in the magnetic susceptibilities of rock units. Modern methodologies and efficient rapid algorithms are used for inverting surface magnetic anomalies to geologically plausible models. In this work, along measured two profiles, AA" and BB', the subsurface is assumed to be subdivided into a large number of cells or blocks, each with unknown magnetic susceptibility (k). This model is subjected to a tomographic inversion process using the Occam inversion procedure (Constable, 1987) to retrieve the possible distribution of the magnetic susceptibilities along the 2D profile as shown in Fig. 3a, b. The equation used for the inversion (uses the depth weighting to overcome erroneous shallow depth bodies, also covariance matrix for smoother model) is given as:

$$\left(A^T W^T WA + \mu C^T C\right)\Delta \mathrm{m} = A^T W^T \Delta f - \mu C^T \mathrm{Cm} \quad (1)$$

where $\boldsymbol{A}$ is the kernel matrix that is related directly to the mesh design or the constructed subsurface model, W is the weighting matrix that minimizes the distortion of $\boldsymbol{A}$ with increasing depth, C smoothing operator, m the model parameter vector, µ—regularizing parameter, and Δf is the vector of residuals between the observed and calculated values. The Occam inversion algorithm is used to model the subsurface and minimize the difference between the observed and the modeled field based on the formula in Eq. (1). Moreover, the Euler deconvolution (Thompson 1982) is applied along the profiles to estimate possible locations and depths to magnetized targets, which are posted on the tomographic model as black dots, indicating the different depths of sources. The Euler's homogeneity equation in two dimensions (2D) (Reid et al. 1990) is expressed as:

$$\left(x - x_o\right)\frac{\partial T}{\partial x} + \left(z - z_o\right)\frac{\partial T}{\partial z} = N(B - T) \quad (2)$$

where $T\,(x, z)$ is the total magnetic field in Cartesian coordinates, (x_0, z_0) the coordinates of the source, N is the structural index, and B is the regional field (Thompson 1982).

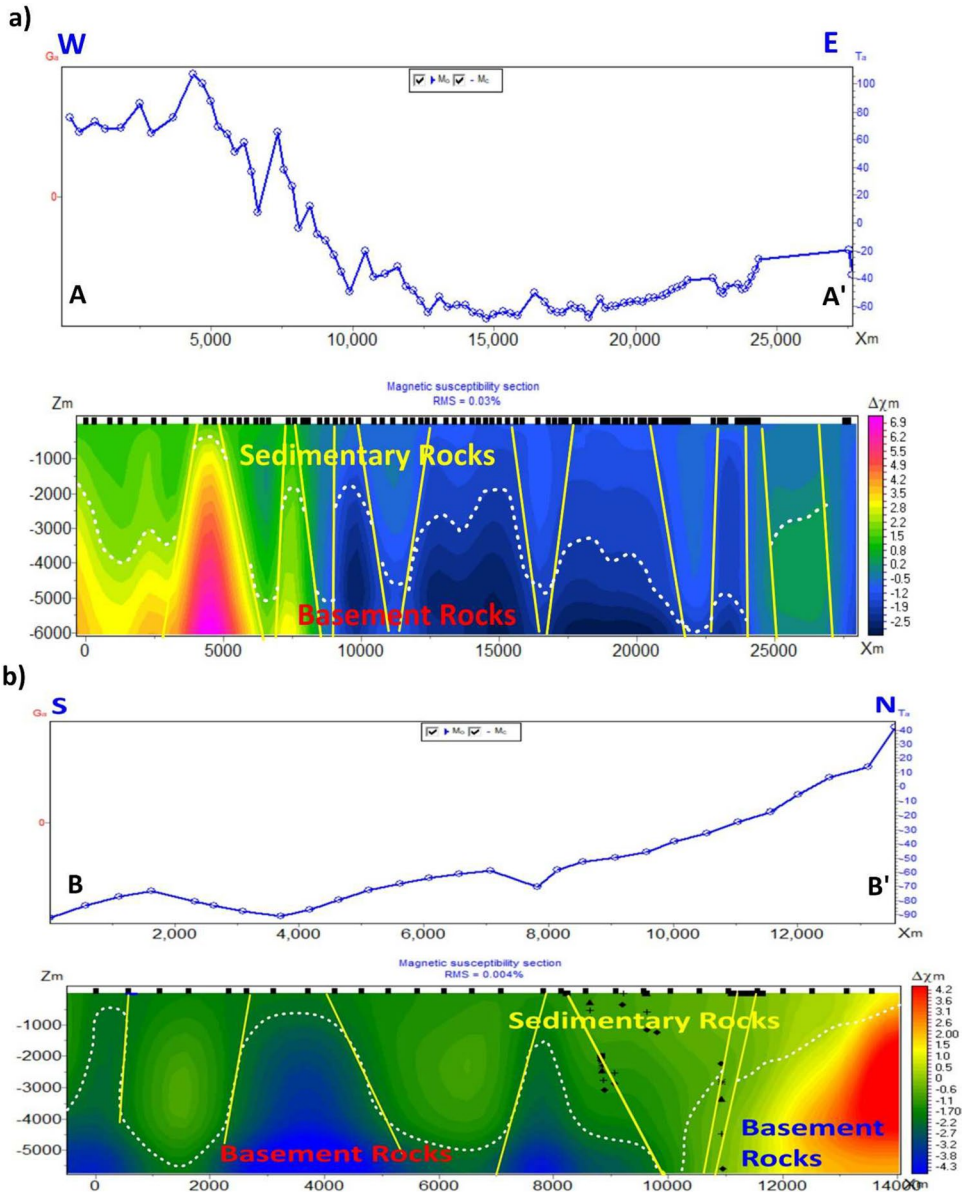

Fig. 3 Tomographic inversion results for the land magnetic profiles. **a** Profile A-A', and **b** Profile B-B'. Black dots indicate calculated Euler deconvolution depths, yellow lines are the expected faults, and white dotted line indicates the possible basement surface

The inverted models of the profiles are shown in Fig. 3. The total length of the profile AA' reaches 28 km, while that of BB' is 14 km cutting the different structural units. The Zondgm2d software is used for the inversion process. The resulting tomographic sections represent the possible distribution of the subsurface magnetic susceptibilities along the two profiles. Each profile is projected to a central straight line that best fits the original one. This process is necessary for preparing the data for inversion along a regular array of data. Blue colors are used to indicate low susceptibility contrast ratings, whereas red and pink colors indicate high values. Using a K-20 magnetic susceptibility meter, surface magnetic susceptibilities are also measured along the profile. The inverted profile is constrained by the observed magnetic susceptibilities, which are employed as *a prior* information.

Profile AA' (Fig. 3a) is running parallel to the Wadi axis. Two types of basement rocks with different magnetic susceptibilities can be recognized. The depth to the basement varies from 2 km at the west to 5 km close to the Gulf of Suez. Tomographic inversion shows an increase in effective magnetic susceptibilities in the western direction in the first 7 km from the measured profile than the eastern direction. The increase in the magnetic anomalies and hence the subsurface magnetic susceptibilities may be related to the ferruginous characteristics of the Nubian Sandstone aquifer as the stratigraphical and microfacies analyses indicate. Possible contact is indicated as a dotted line separating the sedimentary rocks from the basement rocks. This is determined according to the large difference in the susceptibility contrast observed at this level. Consequently, the expected aquifer

is geometrically controlled by the basement topography as indicated by the solid lines representing possible faults along the profile. The thickness of the aquifer increases toward the east and decreases toward the west. Magnetic contacts are observed with the sedimentary succession. Fractures may descend the basement and/or the sedimentary cover.

Profile BB' (Fig. 3b) is similar to AA'. It runs from south to north crossing the Wadi. It reflects the same features as profile AA". The sedimentary rocks to the north are characterized by relatively high magnetic susceptibility contrast in comparison with the low susceptible basement which may be composed of granitic rocks. The depth to the basement is shallow toward the south and increases to the north. This is indicated by Euler solution depths that is represented as black dots. The section is controlled by many faults that are nearly striking north–south.

In summary, the magnetic inversion shows that the aquifer is highly structurally controlled. The thickness of the aquifer increases toward the east and decreases toward the west. Magnetic contacts are observed within the sedimentary succession.

Stratigraphical and microfacies analyses

Stratigraphic setting

The lithostratigraphy of the studied Phanerozoic Erathem is established based on field investigations, rock description, sedimentary structures, stratigraphic contacts, and fossil contents. The oldest exposed rocks in the Wadi Araba are represented by Rod El Hamal Formation of Carboniferous age, which is unconformably overlined by the Qiseib Formation (Permo-Triassic), Khashm El Galala Formation (Jurassic) and Malha Formation (Lower Cretaceous). These rock units are equivalent to the subsurface Nubia Group in the Gulf of Suez province. The upper Cretaceous Galala Formation is exposed along the two borders of the Wadi Araba (Fig. 2).

The Carboniferous Rod El Hamal Formation (Carboniferous age) forms the main bedrock of the eastern part of Wadi Arab. It consists of five succeeded blocks of about 250 m (Fig. 4). The lower 70m is composed of sandstone, yellow, moderately hard cross-bedded, and pebbly, with the thin lamina of shale and siltstone intercalations (Fig. 5A), followed by fossiliferous mixed carbonate-siliciclastic sediments of about 40 m. Pebbly, cross-bedded sandstones with mudstone and limestone intercalation, is the main constituent of the upper part of the formation (Fig. 5B). Many fossils of Carboniferous age are encountered in the field and under a microscope with the sediments of this formation, e.g., corals (*Amygdalophylloides ivanovi* and *Bothrophyllum pseudoconicum*), brachiopods, echinoderms, and foraminifers (Fig. 6G–H). This formation is coeval to Um Bogma Formation in Sinai, the Gilf Formation at Aswan, the subsurface Desouqy Formation of Egypt, the M'rar Formation in Libya and the Berwath Formation of Saudia Arabia (Kora 1998).

The Permo-Triassic red beds of the Qiseib Formation unconformably overlain the Rod El Hamal Formation. This formation is widely distributed in the Wadi (Fig. 2), which is represented by about 100m, from reddish yellow, cross-bedded pebbly sandstones with varicolored mudstone intercalations (Figs. 4 and 5C). Yellow orange dolostone thin beds with badly preserved fossils are noted in the middle part of the formation in some places. The Qiseib Formation is widely distributed in the Easter Desert and Sinai of Egypt, the Amanus Sand of Syria and the Unayzah Formation of Saudi Arabia (Kora 1998).

The Jurassic Khashm El Galala Formation was exposed due to faulting as a small block (20m) at the eastern entrance of the Wadi. It consists mainly of marine sediments greenish shale and marl with limestone intercalations (Fig. 4).

The best exposures of the lower Cretaceous Malha Formation appear at the base of the borders of Wadi Araba (Fig. 2). It consists of about 140m, from non-marine friable, cross-bedded, coarse-to-fine-grained sandstones and kaolinitic mudstone interbeds with occasional marine layers at the upper part (Figs. 4 and 5D). It is widely distributed in Sinai, Eastern and Western Deserts of Egypt and equal to Abu Ballas Formation in Aswan.

The upper Cretaceous Galala Formation represents the carbonate-dominated facies (120m) in the studied area (Fig. 4). Its basal part is characterized by yellowish-green clastic sediments of sandstone, siltstone, and shales. Most succession is composed mainly of fossiliferous, thin-bedded to massive, dolomitic limestones and marls (Fig. 5F–H). These sediments encountered many shallow marine faunas of upper Cretaceous age from echinoderms (*Hemiaster cubicus*), pelecypods (*Ilymatogyra Africana*), cephalopods (*Mammites nodosoides*), corals, and foraminifers (Fig. 7A–F). Galala Formation was recorded in different localities in the Eastern Desert and is equal to the Raha Formation in Sinai of Egypt (Kora et al. 2001). Unconformably, it succeeded by the Eocene carbonate-dominated rocks of Thebes and Mokattam formations.

A thin layer of the quaternary deposits covers most parts of the Wadi Araba (Fig. 2). The grain size of these siliciclastic sediments varies from gravel-, sand-, silt- and mud-sized. It is represented by Wadi deposits, Aeolian dunes and sheets.

Microfacies analysis

In addition to stratigraphic features and sedimentary structures, petrographic examination and microfacies analysis are carried out to delineate the characteristics and quality of the shallow aquifers in the Wadi Araba area. The encountered

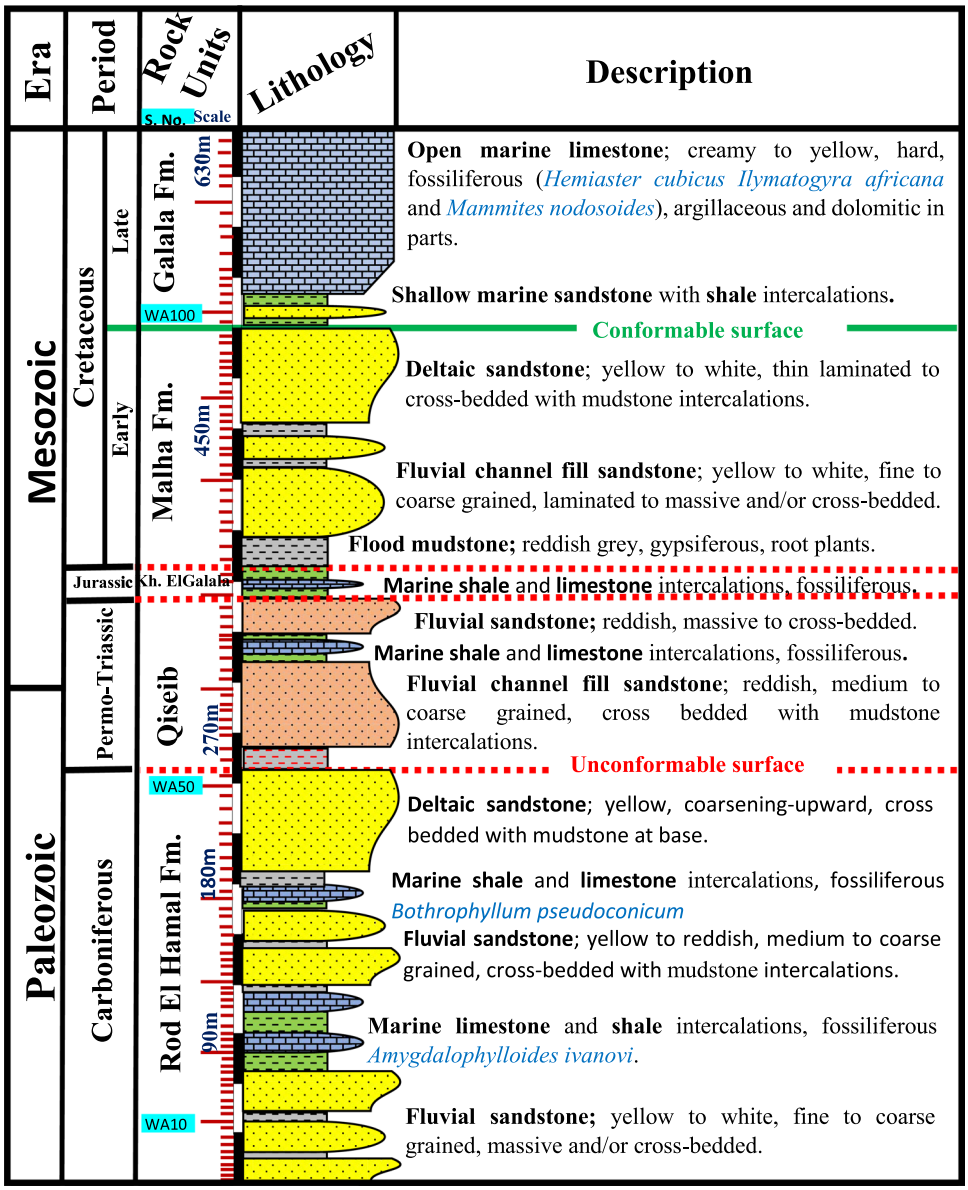

Fig. 4 Composite lithostratigraphic chart of the exposed Carboniferous–Cretaceous systems with prevailed sedimentary facies and depositional environments in the Wadi Araba area, western Gulf of Suez, Egypt

siliciclastic and carbonate microfacies and their diagenetic processes are briefly described and discussed below:

Quartz arenite The sandstones of the quartz arenite microfacies are characterized by white to pale yellow color, friable to soft, and massive to planner cross-bedding. Microscopically, it is composed mainly of quartz grains representing 96% of the rock materials. The quartz grains are medium to coarse-sized, rounded to subrounded, and moderately to well-sorted and corroded and cracked in parts (Fig. 6A–C). Most of the quartz grains are monocrystalline, but there is polycrystalline undergoing undulate extinction. About 4% of the rock constituents consist of iron oxides, glauconite, chert, stable heavy minerals, zircon, and tourmaline. As shown in Fig. 5C silica overgrowth, calcareous and ferruginous coatings are the main cement materials. The blue dye in the thin sections represents the intergranular porosity which reached about 18–20% of the rock volume of the shallow aquifers.

Subarkose Petrographically, subarkose microfacies are made up of quartz grains which form about 85% of the rock materials and more than 10% of different types of feldspars and other rock fragments (Fig. 6D, E). Other grains are also recorded as iron oxides, opaque minerals, glauconite, mica chlorite, and zircon. The subangular and subrounded quartz grains are mono- to polycrystalline, cracked, and moderately sorted. Most alkali feldspar, plagioclase, biotite, chlorite, and glauconite minerals are subjected to alterations and partial dissolution (Fig. 6E) causing secondary porosity

Fig. 5 Field photographs of the Carboniferous– Cretaceous systems in the Wadi Araba area, west Gulf of Suez, Egypt; **A**, **B**—shallow marine and deltaic sandstones of the Carboniferous Rod El Hamal Fm., yellow triangulars refer to fining- and coarsening-upward, respectively, blue arrows refer to cross-bedding, red arrows refer to NE fracture system, hummer for scale; **C**—Fluvial (flood plain and channel fill) sandstones of the Permo-Triassic Qiseib Fm., red arrows refer to NW fracture system; **D**—Exposed coarsening-upward fluvial sandstones of lower Cretaceous Malha Fm. near RIGWA boreholes west Wadi Araba; **E**—RIGWA boreholes; **F**—Fractured open marine limestone of upper Cretaceous Galala Fm.; **G**, **H**—St. Antony and Enaba springs respectively within fractured limestones of Galala Fm

in Wadi Araba aquifers. Scattered altered biotite and hornblende flakes are also observed. All these rock materials are cemented by ferruginous and/or calcareous matrices.

Sublitharenite These microfacies are characterized by gray to brownish-yellow cross-bedded pebbly sandstone, which is recorded in all studied rock units of the shallow Nubian aquifers. It consists of quartz grains (75–83%) and rock fragments (about 20%) as shown in Fig. 6F. The mono- and polycrystalline quartz grains are poorly to moderately sorted and angular to subrounded in shape. The recorded rock fragments consist mainly of old sedimentary sediments, e.g., shales, limestones, and cherts. Some iron oxides, glauconites, and heavy minerals are observed within the facies. The different types of rock materials are embedded in the fine matrix and ferruginous or calcareous cement. The porosity within such facies resulted from different diagenetic processes such as compaction, ferruginous cement, fracturing (Fig. 6F), dissolution, and dolomitization (Fig. 6E).

Greywackes The greywackes microfacies characterize the clastic sediments of the floodplain fluvial deposits of the Nubian sandstone aquifers. These immature, poorly sorted microfacies are composed mainly of pebbly to sand-sized fragments ranging from 70 to 75% of rock materials embedded in a fine-grained matrix (Fig. 6H). These

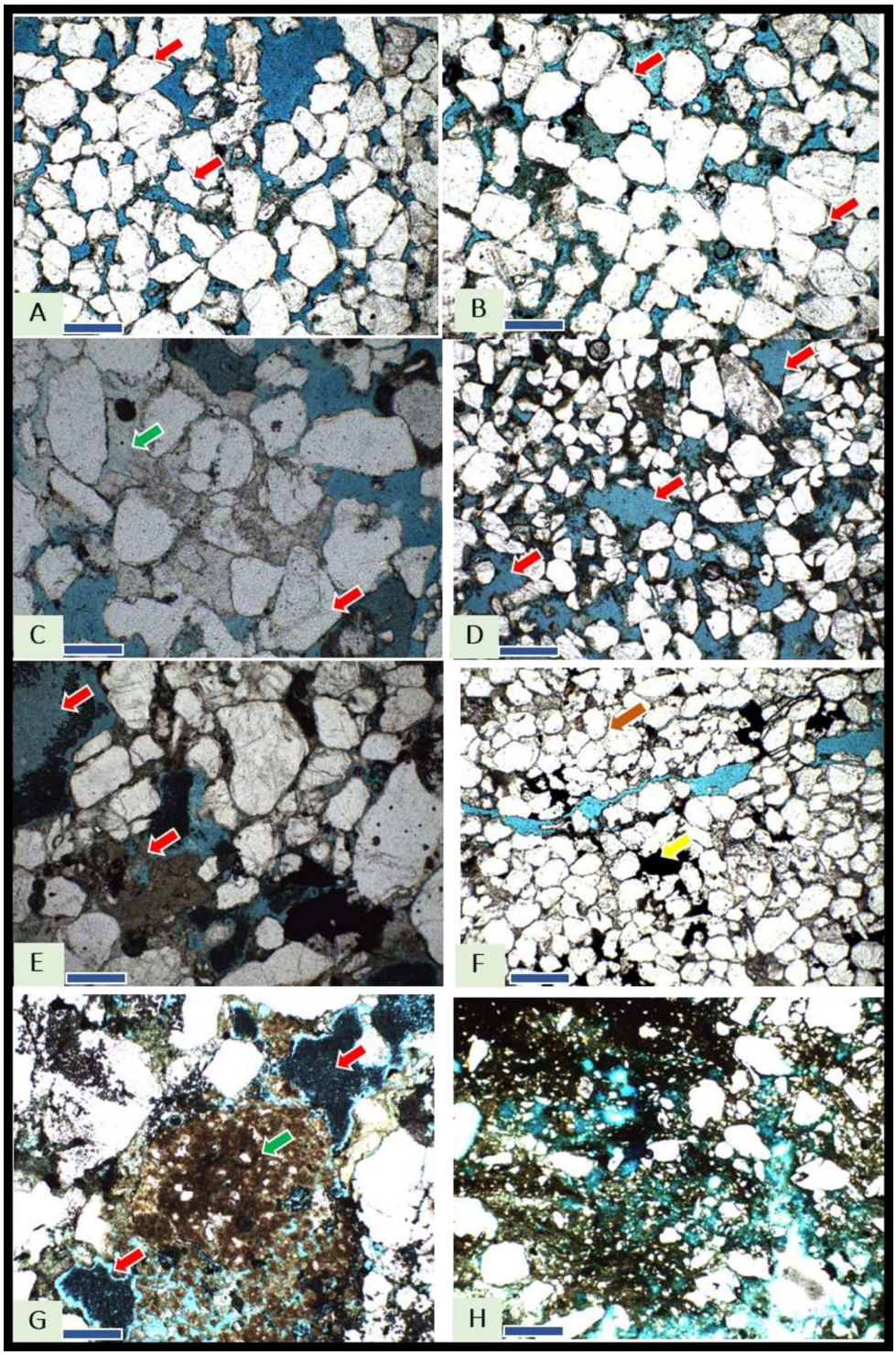

Fig. 6 Microscopic photographs of sandstone microfacies of the Nubia Group at Wadi Araba area; **A**–**C**—Quartz arenite of Rod El Hamal (WA7), Malha (WA77) and Qiseib (WA55) formations, respectively, red arrows refer to quartz overgrowth and green one refers to carbonate cement; **D**, **E**—Subarkose of Rod El Hamal Fm. (WA3, WA45), moderately sorted, red arrows refer to partial to complete dissolution of mafic minerals; **F**, **G**—Sublitharenite of Rod El Hamal Fm. (WA21, WA32), poor to moderately sorted, brown arrow refers to concavo-convex contacts between quartz grains, yellow to iron cement, red arrows to partial dissolution of rock fragments, and green to dolomitization. **H**—Greywacke microfacies of Qiseib Fm. (WA67), the blue color indicates porosity. All figs under PPL. Blue bar = 1mm

mixed facies consist of angular to subrounded polycrystalline quartz, altered feldspars, and cracked rock fragments. Besides the clayey matrix, the graywacke fragments are cemented by ferruginous and/or calcareous material. The blue color of the Fig. 6H refers to porosity within aquifer rocks.

Mudstone/Wackestone microfacies It is a common carbonate microfacies that constitutes about 90% of the shallow carbonate aquifers of the studied area. The limestones of these facies are white to yellow in color, thin-bedded, fossiliferous, dolomitic, and fractured. Microscopically, it is composed of several types of allochems (up to 40%)

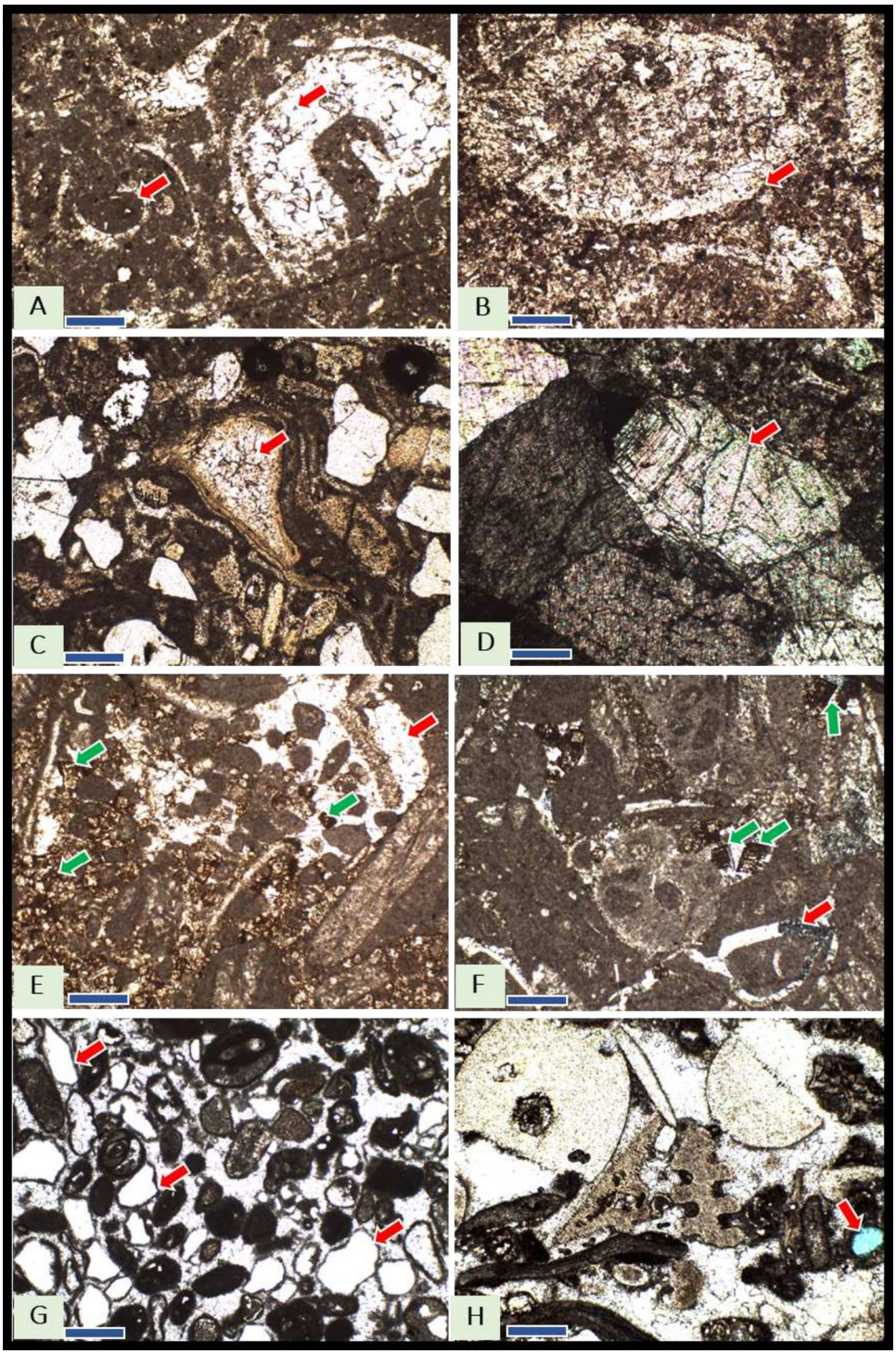

Fig. 7 Microscopic photographs of limestone microfacies of the Galala Fm. (**A** to **F**) and Rod El Hamal Fm. (**G** and **H**) at Wadi Araba area; **A**, **B**—mudstone (biomicrite) red arrows refer to recrystallization of shell fragments (WA109). **C**, **D**—sandy wackestone (biomicrite), shell fragments filled with sparry calcite (red arrows) (WA103). **E**, **F**—Packstone (Dolomitic intrabiosparite) allochems imbedded in sparite (red arrows), which subjected to dolomitization in most parts (green arrows) (WA114). **G**—Grainstone (sandy pelbiosparite) (WA27) quartz grain coated by thin micritic film (red arrows). **H**—Grainstone (biosparite) (WA41) red arrow refers to partial dissolution of shell fragments (intragranular porosity). **D** and **H** under PLX, other under PPL. Blue bar = 1mm

from bioclasts (e.g., pelecypods, gastropods, corals), peloids, and aggregated grains (Fig. 7A–D). Some detrital silt to sand-sized quartz grains is observed within the facies. All these carbonate grains are embedded in a micritic and/or calcitic cement. Whoever, the shell fragments of these microfacies were replaced and/or filled by calcite minerals. Some calcite minerals recrystallized to form sparry calcite as shown in Fig. 7D

Packstone/Grainstone microfacies In the field, the carbonate sediments of these facies are characterized by massive to planar cross-bedded, dolomitic with fenestra and/or porous

fabrics. Petrographically, it consists mainly of well-sorted different allochems from bioclasts, ooids, peloids, intraclasts, and aggregated grains with detrital quartz grains (Fig. 7E–H). The allochems represent about 90% of the rock constituent and are tightly packed and cemented by sparry calcite. The bioclasts are mainly represented by molluscans, bryozoans, foraminifera, algae, and echinoid plates. The main diagenetic processes recorded in the present facies are dolomitization, recrystallization (Fig. 7E, F), micritization (Fig. 7G), and dissolution (Fig. 7H) which formed a secondary type of porosity with the carbonate aquifers.

Diagenetic processes and rock porosity

As soon as the sediments of the studied area were deposited, they were subjected to different diagnostic physical, chemical, and biological processes. The most common diagenetic processes are compaction, cementation, recrystallization, dolomitization, dissolution, pressure solution, fracturing, and leaching out. Diagenetic processes played an important role in the aquifer porosity, and permeability as well as groundwater chemistry and quality.

Compaction, cementation, recrystallization, micritization, and pressure solution are the principal processes leading to porosity reduction in the shallow aquifers of the studied area. Concavo-convex contacts, cracking and corrosion of the quartz grains refer to compaction (Fig. 6F). According to Graton & Fraser, (1935), compaction can reduce the sandstone porosity to 26%. In most cases, calcareous (Fig. 6C), ferruginous (Fig. 6F), and micritic cement filled the pore spaces, vugs, and fractures. Moreover, silica overgrowth (Fig. 6A, B) and micrite and/or clay mineral coating (Fig. 7G) are recorded in many microfacies. However, all these processes lead to reducing rock porosity. The main source of silica and clay minerals resulted from the alteration and pressure solution of feldspar minerals (Bjorkum et al. 1993). Dolomitization is a process whereby limestone or its precursor sediment is completely or partly converted to dolomite by the replacement of the original $CaCO_3$ with magnesium carbonate, through the action of Mg-bearing water.

Several fractures and joint sets were observed in the field (Fig. 5B, C) and in microscopic scales (Fig. 6F) in the sediments which accompanied the tectonic events in the Wadi Araba area. However, these fractures and joints enhanced and increased the porosity and permeability of the studied aquifer forming potential pathways for groundwater movement. Dissolution of many unstable minerals within subarkose (Fig. 6D, E) and sublitharenite (Fig. 6G) of sandstone microfacies and fossil fragments of the carbonate microfacies (Fig. 7H) leads to increasing the inter- and intra-porosity of the studied shallow aquifers. According to Selly (1998), the dissolution process is a very important diagenetic factor for reservoir quality. In most cases, unsaturated groundwater is considered the cause of dissolving the unstable minerals and shell fragments. Moreover, the dissolution of authigenic minerals or grains can enhance porosity as a secondary type (Ehrenberg 1990).

Hydrogeochemistry

Groundwater chemistry is greatly significant in determining the type of water, origin, quality, and suitability for different purposes. It is mainly based on the chemical analysis of the collected water samples from different aquifers and springs in the area (Fig. 1 and Tables 1 and 2). Groundwater at all sites is brackish to saline water according to the classification based on TDS (fresh: < 1000 mg/l, slightly saline: 1000–3000 mg/l, moderately saline: 3000–10,000 mg/l, highly saline: 10,000–35,000 mg/l) suggested by the USGS (2000). The integrated classification of groundwater quality based on TDS and TH is demonstrated in Fig. 8. It can be seen that all groundwater samples belong to the hard brackish and very hard saline categories.

In the histogram chart depicting the distribution of total dissolved solids (TDS) in the two aquifers (Fig. 9a), it is evident that the salinity of groundwater is higher in samples obtained from Southern Galala compared to those from Northern Galala (Upper Cretaceous aquifer). This increase could be attributed to the leaching and dissolution processes of the aquifer limestone occurring during the flow of groundwater. Additionally, the salinity shows a further escalation toward the Gulf of Suez, which is associated with seawater intrusion in the Nubian sandstone aquifer.

The concentration of major cations, including Ca^{++}, Mg^{++}, Na^{+} and K^{+}, in the examined groundwater are detailed in Table 1. Calcium and magnesium ions

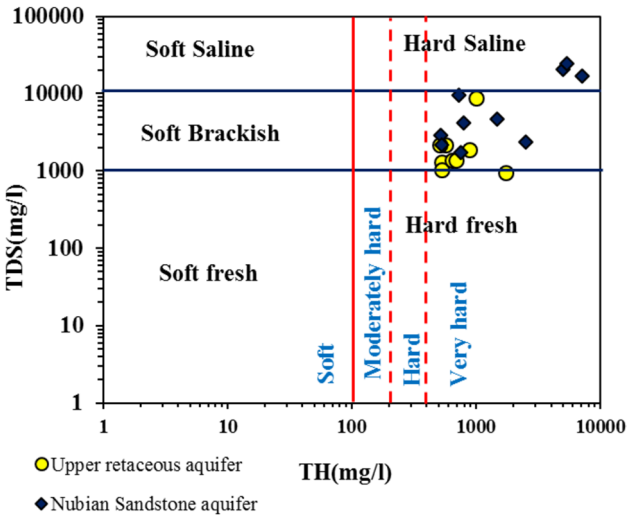

Fig. 8 **a** Distribution of collected water samples and **b** scatter plots of TDS versus TH showing groundwater quality

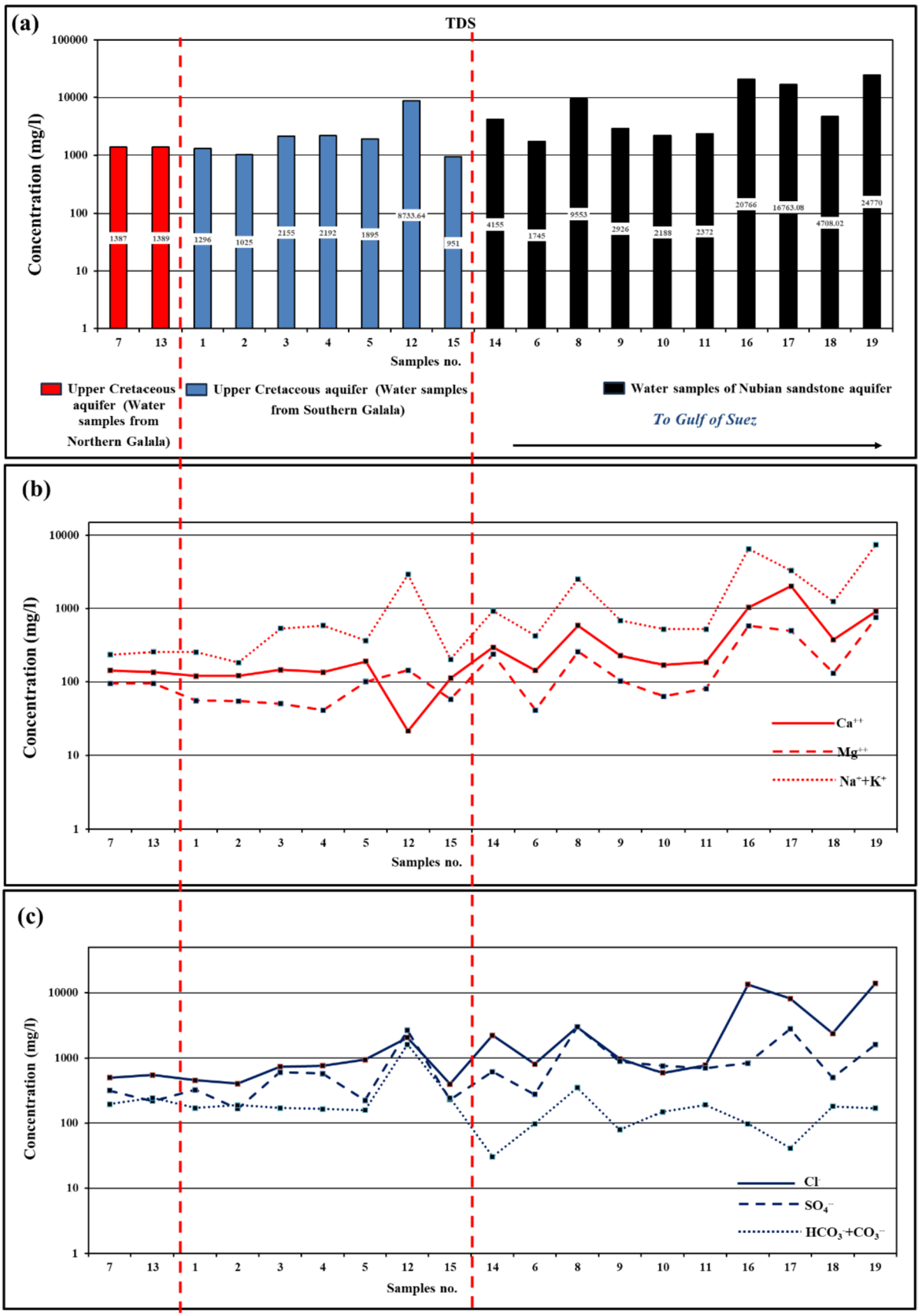

Fig. 9 **a** TDS distribution of collected water samples based on their presence also, **b** Major cations and **c** Major anions

predominantly originate from processes such as calcareous leaching, dolomites, gypsum, and anhydrites. Additionally, calcium ions result from the cation exchange cycle (Garrels 1976). The Ca^{++} concentration exhibits variability, ranging from 21.4 mg/l for sample 12 to 2010.3 mg/l for sample 17, with an average of 371.6 mg/l (Table 1 and Fig. 9b). Magnesium concentration varies from 41.1 mg/l in sample 6 to 751.3 mg/l in sample 19, averaging 181.1 mg/l (Table 1 and Fig. 9b).

Sodium, a crucial ion in natural water due to its impact on soil structure and its direct association with salinity primarily occurs in clay minerals and evaporates. Sodium concentration spans from 180 mg/l in sample 2 to 7200 mg/l in sample 19, averaging 1527.4 mg/l (Table 1 and Fig. 9b). Potassium, derived from K-feldspar weathering and aquifer matrix clay minerals, has lower concentration in groundwater compared to sodium, as potassium minerals exhibit greater resistance to weathering (El-Aziz 2017). The concentration of potassium ranges from 3 mg/l in samples 1, 2, 7, 10, 11, and 15 to 264 mg/l in sample 19, with an average of 29.3 mg/l (Table 1 and Fig. 9b).

The primary anion, chloride, originates from the dissolution of sodium chloride in rocks and soil within water. It serves as a significant indicator of groundwater quality, with its concentration increasing in groundwater when combined with wastewater or seawater (Deshpande and Aher 2012). The chloride concentration in the investigated groundwater ranges from 13946.8 mg/l in sample 19 to 397 mg/l in sample 15, averaging 2793.2 mg/l (Table 1 and Fig. 9c).

Sulfate is chiefly derived from sedimentary rocks, particularly gypsum, anhydrite, and certain types of shales. The measured sulfate concentration varies from 166.3 mg/l in sample 2 to 3001.2 mg/l in sample 8, with an average of 909.6 mg/l (Table 1 and Fig. 9c). Bicarbonates, likely originating from the dissolution of carbonate sediments, play a role in groundwater composition. Another potential source is the rapid dissolution during initial infiltration, as soil produces CO_2, which dissociates into carbonic acid, impacting the groundwater's ability to dissolve calcium carbonate (Dyke 1999). The presence of bicarbonates ranges from 30.5 mg/l in sample 14 to 1327.2 mg/l in sample 12, with an average of 216.6 mg/l (Table 1 and Fig. 9c).

In general, the spatial trend of the concentration changes of ions like TDS. Ion concentration in carbonate aquifer is higher in southern Galala Springs compared to Northern Galala. Ion concentration of the Nubian Sandstone Aquifer is higher than that of the carbonate and increase toward the Gulf of Suez. The higher concentration in sandstone aquifers could be related to seawater intrusion and or evaporation (Salem and Osman 2017a, b; Hasan et al. 2023 and Salem et al. 2021a and 2022a). Carbonate concentrations carry the aquifer lithology impact. Although the higher TDS and ions concentrations in the sandstone aquifer, the higher concentration of carbonate ions were recorded in the carbonate aquifer which might related to dissolution processes (Abdelazeem et al. 2021).

Samples classification

Statistical classification The studied groundwater samples were classified into five groups to describe the characteristics of each group of samples according to the degree of similarity between the groundwater samples with respect to each other which depends on the major ion concentration in meq/l (Figs. 10 and 11). Table 3 presents the average values of hydrochemical data for each group.

Samples from group A (samples 16. 17 and 19) have the highest TDS average value (20,766 mg/l) and Na^+–Cl^- groundwater type ($Na^+ + K^+ > Ca^{++} > Mg^{++}$ and $Cl^- > SO_4^{--} > HCO_3^-$) (Table 3, 4 and Fig. 11). These samples belong to Nubian Sandstone aquifer and of high salinity as it is affected by the seawater intrusion from Gulf of Suez. Samples from group D (samples 1, 2, 7, 13, and 15) have the lowest TDS average value (2127.4 mg/l) and Na^+–Cl^- groundwater type ($Na^+ + K^+ > Ca^{++} > Mg^{++}$ and $Cl^- > SO_4^{--} > HCO_3^-$) (Tables 3, 4 and Fig. 11). These samples belong to Upper Cretaceous aquifer and its low salinity could be related to rainwater source. Samples from groups B, C, and E (samples 3, 4, 5, 6, 8, 9, 10, 11, 12, 14, and 18) have TDS average values of 9143.3, 4431.5, 2210.4 mg/l, respectively, and of Na^+– Cl^- groundwater type ($Na^+ + K^+ > Ca^{++} > Mg^{++}$ and $Cl^- > SO_4^{--} > HCO_3^-$) for groups C and E but Na^+– SO_4^{--} groundwater type ($Na^+ + K^+ > Ca^{++} > Mg^{++}$ and $SO_4^{--} > Cl^- > HCO_3^-$) for group B (Tables 3,4 and Fig. 11).

Higher silicon concentration in samples of groups A, B, and C could be related to the clastic facies of the aquifer where most samples of the three groups belong to the Nubian sandstone aquifer. Al, Fe, and Mn are the most abundant trace elements in the investigated groundwater, and their average concentration (mg/l) in the four groups, respectively, are (0.19, 0.11, 0.21, 0.25, and 0.12), (3.53, 0.103, 1.05, 0.05, 0.01) and (0.73, 0.11, 5.45, 0.02 and 0.01). Encountered higher Fe and Mn could be related to the ferruginous characteristics of the Nubian Sandstone aquifer.

Graphical classification The groundwater samples labeled according to their respective group of HCA (Fig. 11) were presented in the Piper diagram (Fig. 11). Na^+ is the major cation in the majority of the groundwater samples and Cl^- is the main anion. In the right triangle, SO_4^{--} increases to reach its maximum concentration in groups B and E (samples 3, 4, 5, 6, 8, 9, 10, 11, and 12). In the left triangle, Ca^{++} and Mg^{++} increase, while Na^+ decreases indicating ion exchange where Ca^{++} and Mg^{++} replace Na^+, especially in group D (samples 1, 2, 7,

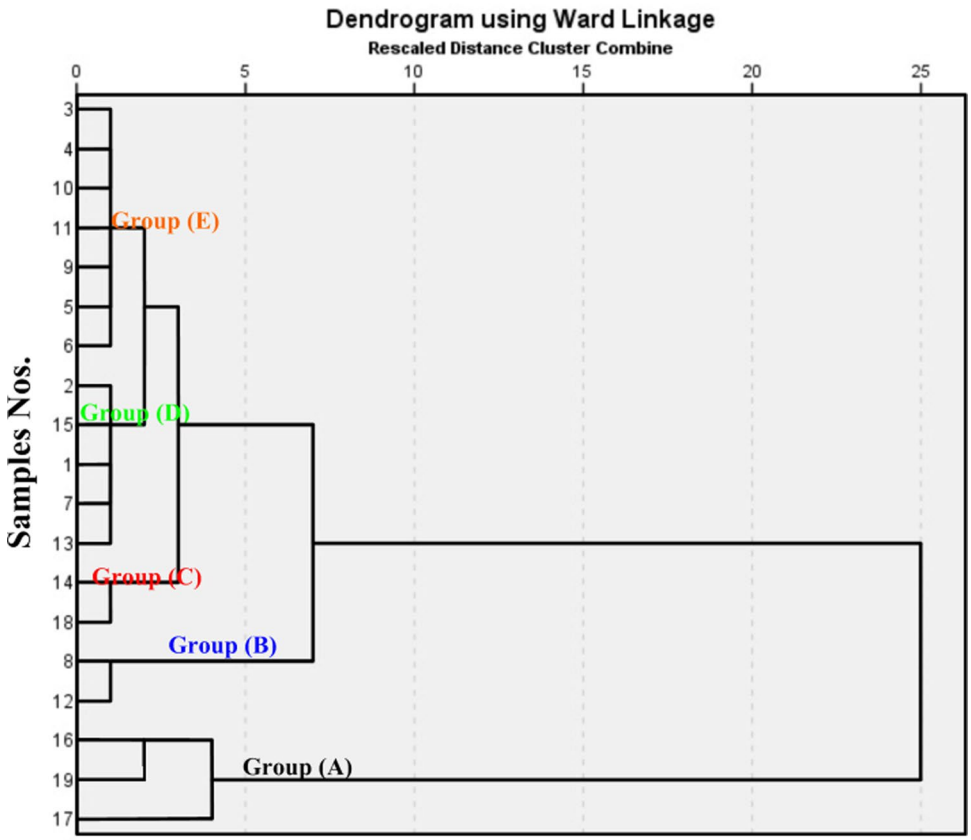

Fig. 10 Dendrogram shows the grouping of the groundwater samples into five groups depending on the concentration of the ions in mg/l

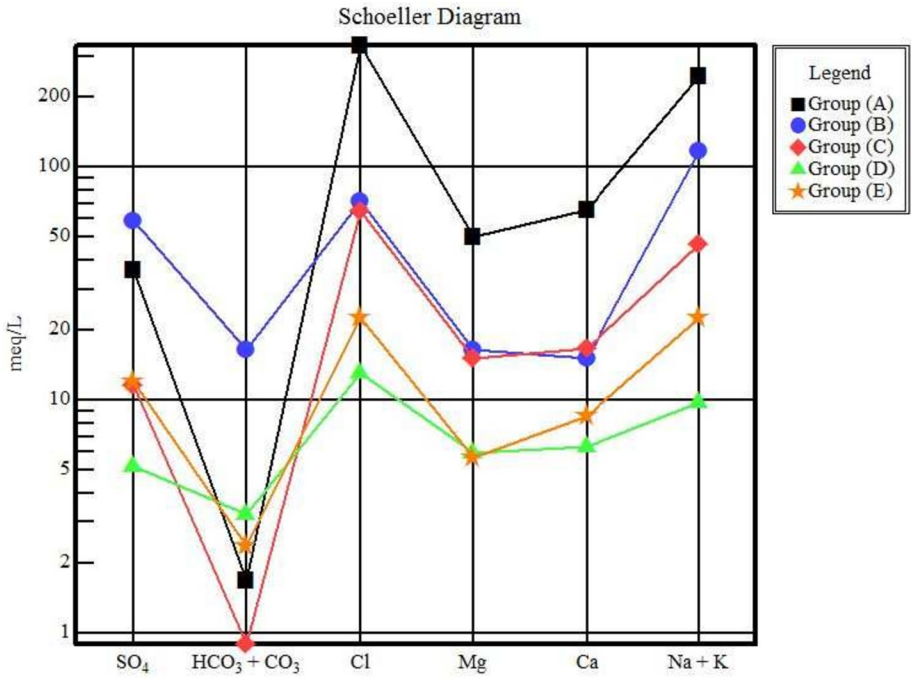

Fig. 11 Schoeller diagram of the obtained groundwater sample groups

13, and 15). Based on general patterns of plotted data of groundwater samples on the diamond field (Fig. 18), the majority of the groundwater samples (68%; samples 1, 3, 4, 6, 8, 9, 10, 11, 12, 14, 16, 18 and 19) occupy the subzone (7) in which the water is characterized by primary salinity where Na^+ and K^+ exceed SO_4 and NaCl salt prevails compared to seawater (Fig. 12) (Rajendra et al. 2009). The other groundwater samples (32%; samples 2,

Table 3 Average composition of the major hydrochemical parameters of the classified groundwater sample groups

Groups	T	pH	EC	TDS	Ca^{++}	Mg^{++}	Na^{+}	K^{+}	CO_3^{--}	HCO_3^{-}	Cl^{-}	SO_4^{--}
Units	°C	µS/cm										
A (samples, 16, 17, and 19)	26.0	8.0	33,503.7	20,766.4	1320.0	609.7	5600.0	138.7	6.8	95.7	11,838.1	1744.3
B (samples, 12 and 8)	23.7	8.4	13,952.2	9143.3	303.0	200.6	2700.0	14.5	159.0	825.8	2527.7	2825.6
C (samples, 14 and 18)	30.8	6.3	7588.5	4431.5	335.5	183.9	1050.0	31.5	0.0	105.9	2303.7	558.0
D (samples, 1, 2, 7, 13, and 15)	22.4	7.6	2127.4	1209.6	125.9	72.1	222.0	3.8	4.8	203.7	461.8	251.3
E (samples, 3, 4, 5, 6, 9, 10, and 11)	20.0	8.0	3767.6	2210.4	170.6	68.8	515.7	4.3	10.5	135.1	797.9	575.1

Table 4 Average composition of the trace elements of the classified groundwater sample groups

Groups	Al	Cd	Co	Cr	Cu	Fe	Mn	Mo	Ni	Pb	V	Zn	Si
Units	mg/l												
A (samples, 16, 17 and 19)	0.19	0.00	0.00	0.00	0.01	3.53	0.73	0.00	0.00	0.00	0.00	0.60	16.61
B (samples, 12 and 8)	0.11	0.00	0.00	0.00	0.00	0.10	0.11	0.01	0.00	0.08	0.03	0.01	18.73
C (samples, 14 and 18)	0.21	0.00	0.00	0.02	0.00	31.05	5.45	0.00	0.01	0.00	0.00	0.69	14.72
D (samples, 1, 2, 7, 13 and 15)	0.25	0.00	0.00	0.00	0.01	0.05	0.02	0.01	0.00	0.07	0.02	0.02	5.94
E (samples, 3, 4, 5, 6, 9, 10 and 11)	0.12	0.00	0.00	0.00	0.00	0.01	0.01	0.00	0.00	0.07	0.01	0.01	4.54

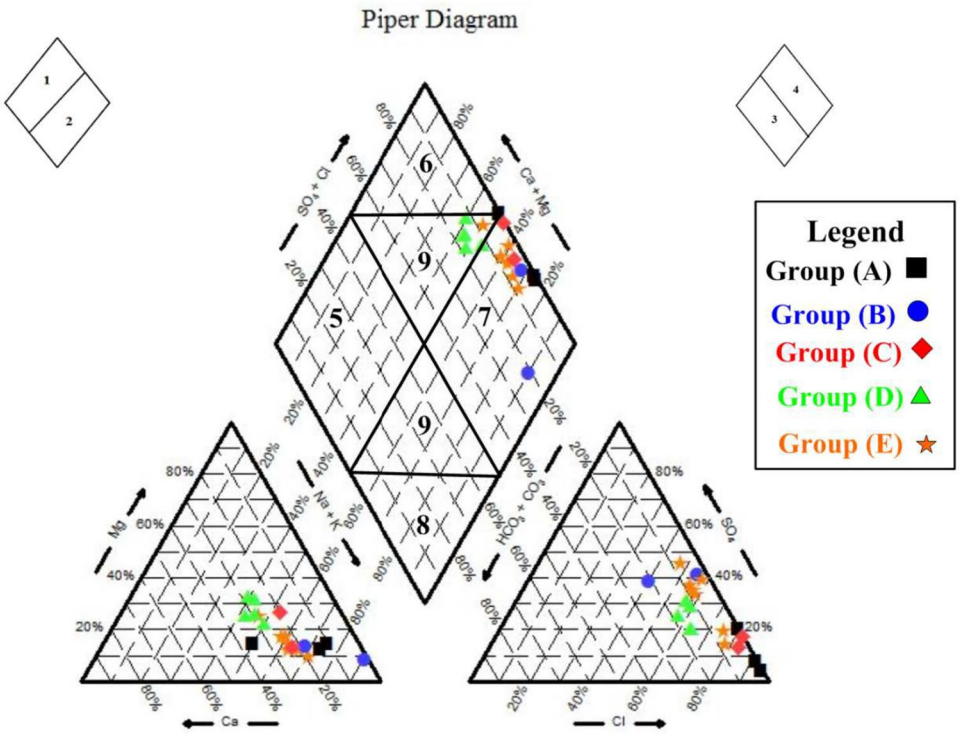

Fig. 12 Piper diagram of the obtained groundwater sample groups

5, 7, 13, 15, and 17) occupy the subzone (9), in which none of the cation–anion pairs exceeds 50% (Rajendra et al. 2009). The plot displays that the chemistry of the groundwater belongs essentially to $CaMgSO_4$ and NaCl.

Ionic relationships

Statistical analysis The dendrograms used for classifying the ion association in the studied groundwater for the two

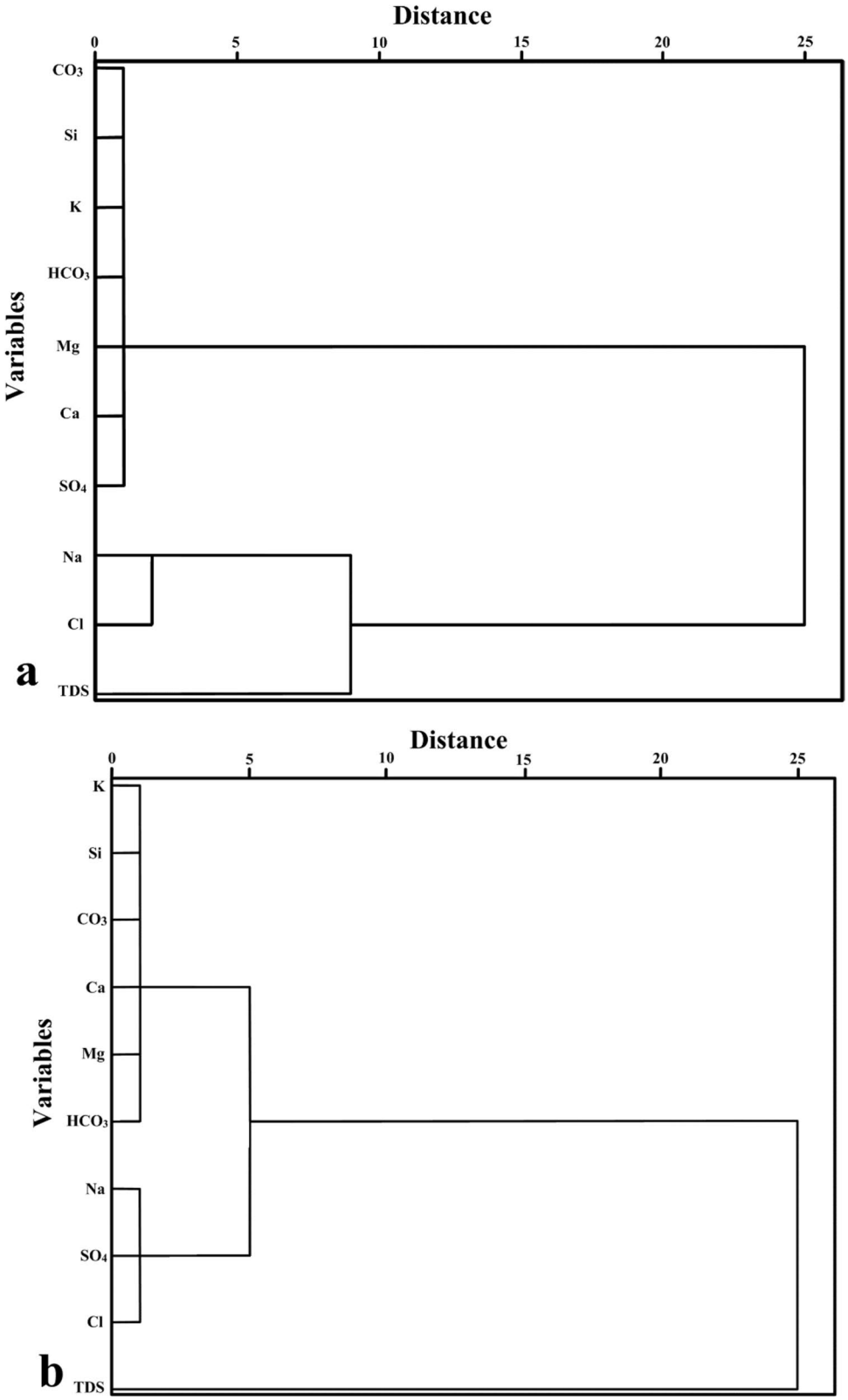

Fig. 13 Dendrograms show the major ion grouping in the Nubian Sandstone groundwater aquifer (**a**) and the Upper Cretaceous aquifer (**b**)

aquifers are shown in Fig. 13a and b. There are two groups of chemicals in the Nubian Sandstone groundwater aquifer system: SO_4–Ca–Mg–HCO_3–K–Si–CO_3 and Cl–Na. The first group could be related to water–rock interaction, and the second is related to either seawater intrusion or evaporation. The SO_4–Ca association is located close to Na–Cl

because either seawater intrusion or evaporation is accompanied by an increase in Ca and SO_4, while the HCO_3–K–Si–CO_3 subgroup is located far from Na–Cl because it is just related to water–rock interaction. Compared to the Nubian Sandstone Aquifer, the Upper Cretaceous aquifer shows two different ion associations: Na–Cl–SO_4 and Ca–Mg–HCO_3–K–Si–CO_3. The association between Na and SO_4 indicates ion exchange between Na of rocks and Ca of dissolved gypsum, while K–HCO_3–Ca–Mg indicates a freshwater source (Salem and Osman 2017a).

Based on Pearson's method**,** the correlation between the groundwater's major chemical variables was determined as shown in Table 5. A strong correlation ($r \geq 0.75$) was recognized between TDS and Ca, Mg, Na, K, and Cl; Na and Cl and K; Mg and Na, Cl and K; CO_3 with HCO_3^-, while moderate correlation (0.75–0.5) was noticed between several water specifications such as between TDS and SO_4 and Si; Ca and Na, K and SO_4; Mg and SO_4; Na and SO_4 and Si; K and Si; CO_3 and SO_4 and Si; HCO_3 and Si. The rest of the relationships are weak (< 0.5). From this analysis, we can conclude that Ca, Mg, Na, K, Cl, and Si are the main component affecting groundwater salinity.

Binary relationships *TDS versus major ions:* The relationships of TDS versus major ions (Ca, Mg, Na, HCO_3, SO_4, and Cl) are shown in Fig. 13. TDS versus Ca relationship (Fig. 14a) is strong ($r = 0.784$, Table 3). Samples related to the Upper Cretaceous carbonate aquifer and the low salinity samples of the Nubian sandstone aquifer are plotted just below the rainwater–seawater mixing line indicating the meteoric origin of Ca in such samples. On the other hand, Ca concentration in the Nubian aquifer samples with higher salinity showed higher values than that of the mixing line which means the addition of Ca either by weathering of silicate minerals or ion exchange with Na (Ibrahim and Lyons 2017). TDS versus Mg, Cl, and Na + K relationships (Fig. 14b, e, and f) are significant with a higher correlation

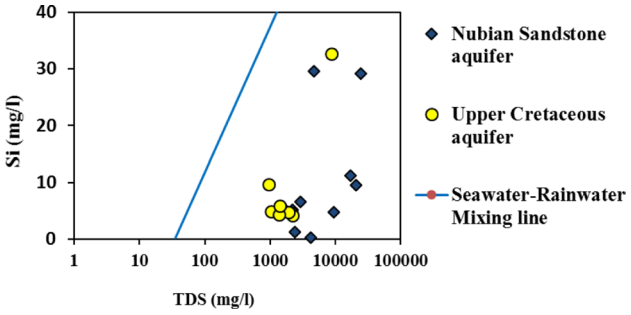

Fig. 14 TDS–Si relationship

coefficient (Table 3). All the samples were plotted below and parallel to the mixing line. This means the increase in Na + K, Cl, and Mg might be related to seawater intrusion or evaporation, especially in the Nubian aquifer samples. Also, ion exchange processes might be responsible for the lower concentration compared to that of the mixing line where Na and K were consumed from the groundwater by ion exchange with calcium (Kumar et al. 2009). The TDS versus HCO_3 and SO_4 relationships (Fig. 14c and d) are weak and intermediate, respectively (Table 5). The samples in the TDS-HCO_3 relationship are mostly clustered around the mixing line while in the TDS-SO_4 relationship sample is plotted mostly under the mixing line. This indicates that the dissolution of gypsum is accompanied by carbonate precipitation (Salem and Elhorieny, 2014). TDS versus Si relationship (Fig. 15) is intermediate ($r = 0.509$, Table 5). If TDS would have resulted from water–rock interaction, a positive correlation between SiO_2 and TDS would have been logically expected (Khan and Umar, 2010).

Na versus Cl: The parameter Na/Cl reflects the inequity of sodium chloride in water. This differs greatly from the difference in maximum dissolved solid concentration. Water is meteoric when this ratio exceeds unity and marine when it is less than unity (about 0.8) (Salem and Osman

Table 5 Correlation coefficient between groundwater parameters

Variables	TDS	Ca^{++}	Mg^{++}	Na^+	K^+	CO_3^{--}	HCO_3^-	Cl^-	SO_4^{--}	Si
TDS	1									
Ca^{++}	0.784**	1								
Mg^{++}	0.976**	0.798**	1							
Na^+	0.981**	0.657**	0.945**	1						
K^+	0.858**	0.570*	0.890**	0.852**	1					
CO_3^{--}	0.114	−0.183	−0.029	0.178	−0.056	1				
HCO_3^-	0.036	−0.261	−0.112	0.11	−0.123	0.965**	1			
Cl^-	0.975**	0.761**	0.976**	0.966**	0.866**	−0.037	−0.112	1		
SO_4^{--}	0.598**	0.577**	0.502*	0.534*	00.322	0.506*	0.452	0.414	1	
Si	0.509*	0.194	0.412	0.547*	0.532*	0.577**	0.570*	0.427	0.41	1

** Correlation is significant at the 0.01 level (two-tailed)

* Correlation is significant at the 0.05 level (two-tailed)

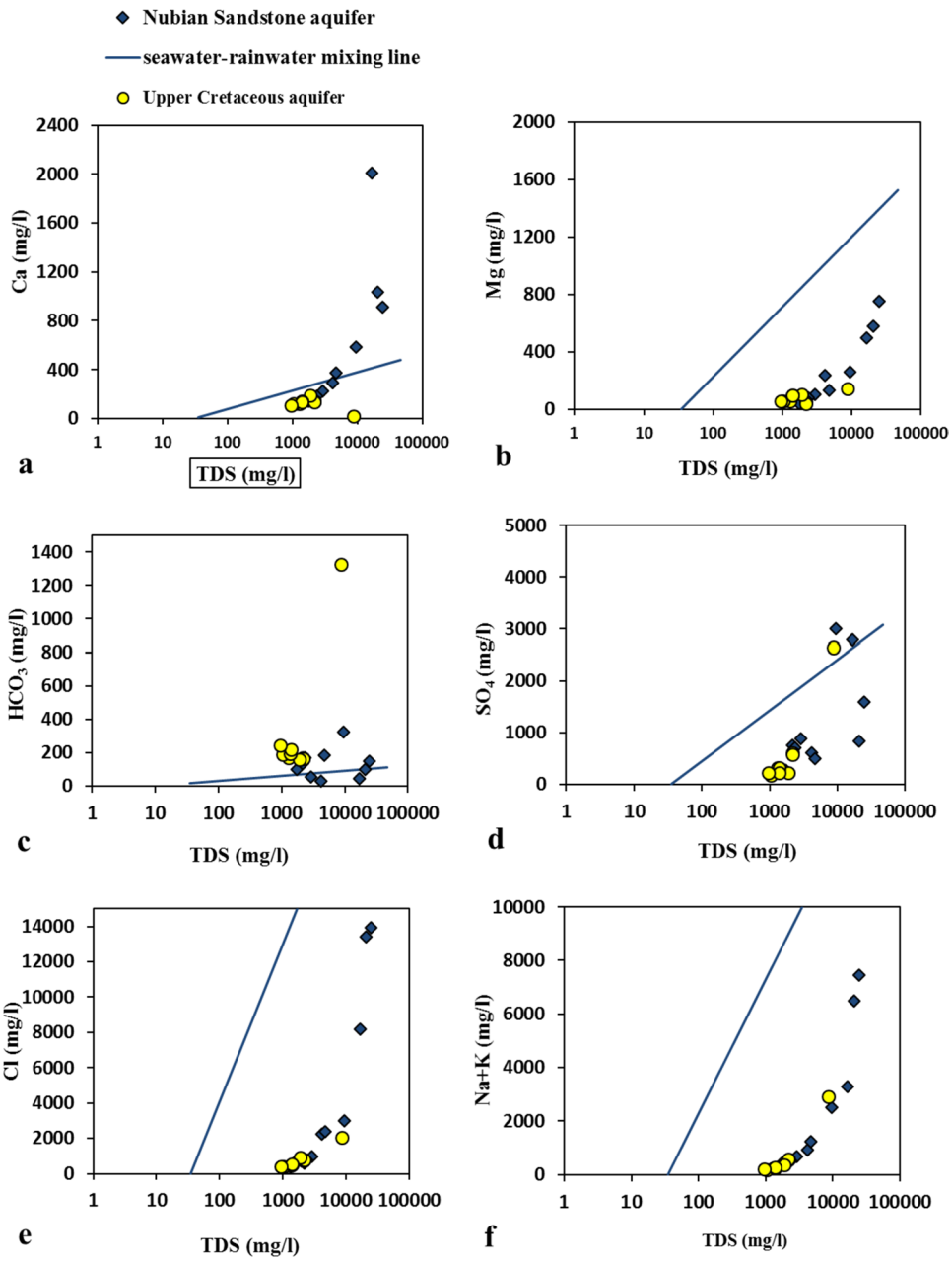

Fig. 15 TDS–major ions relationships

Table 6 Statistical summary of the proposed ionic ratios of the collected samples and that of seawater and rainwater

Sample no	Na/Cl	Ca/Mg	SO_4/Cl	Ca/SO_4	Ca/Cl	Ca/HCO_3	Mg/HCO_3	SO_4/HCO_3
Max	2.26	2.46	0.95	3.12	0.52	151.17	61.56	85.74
Min	0.60	0.09	0.05	0.02	0.02	0.05	0.56	1.12
STDV	0.39	0.55	0.28	0.72	0.14	34.32	16.89	19.35
Average	0.95	1.33	0.44	1.17	0.35	15.17	10.38	11.01
> 1	7	14	0	11	0	18	18	19
> 1%	37	74	0	58	0	95	95	100
< 1	12	5	19	8	19	1	1	0
< 1%	63	26	100	42	100	5	5	0
Seawater	0.88	0.19	0.08	0.39	0.03	13.74	72.09	35.53
Rain water	1.04	5.65	0.73	4.25	3.10	1.05	0.19	0.25

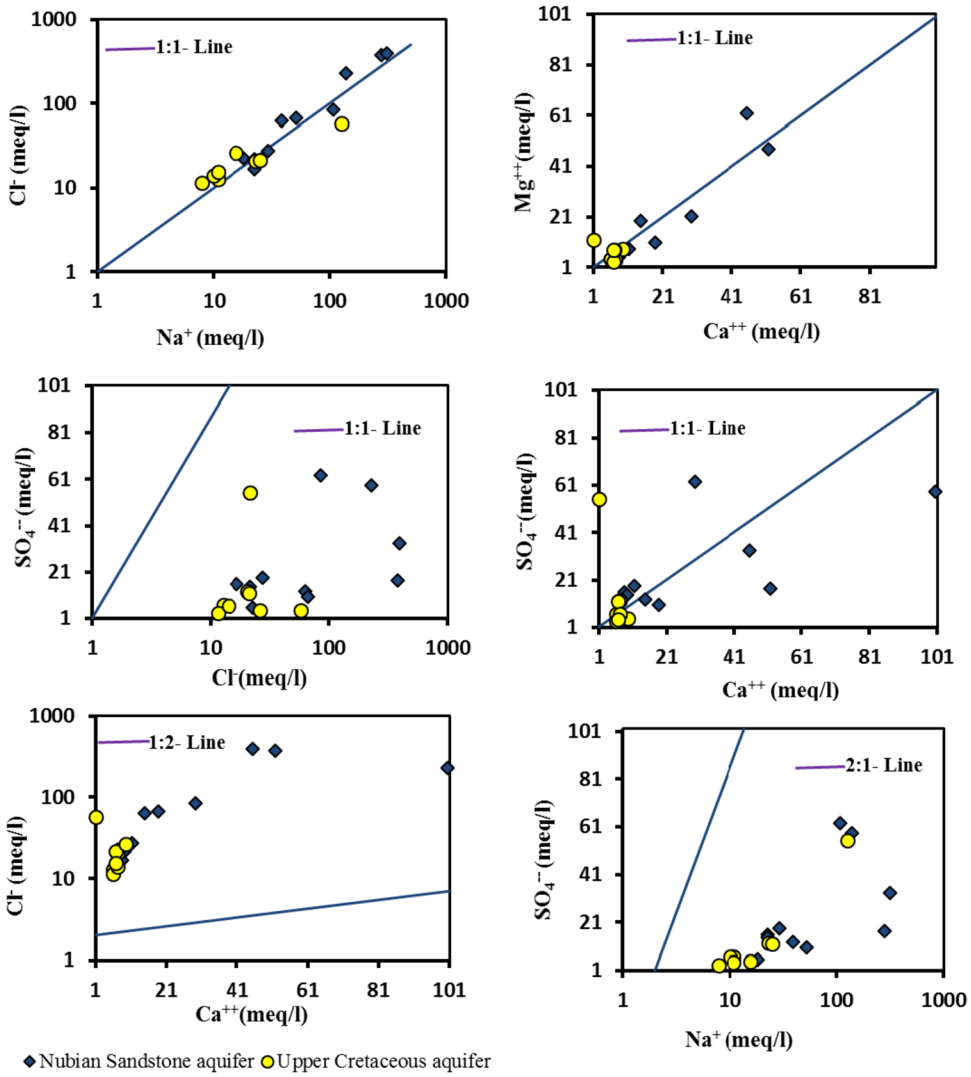

Fig. 16 Ionic relationships to estimate the hydrogeochemical processes that occurred in the studied groundwater

2017b). Most samples (63%) are less than 1 (Table 6) reflecting the marine origin and/or evaporation effect in the groundwater. The samples are plotted in Fig. 16a above and below the unit line. The correlation coefficient (r) is 0.966 (Table 5). Sodium excess could be related to either ion exchange and/or addition from the terrestrial origin (Fisher and Mullican 1997; Lee and Song 2007; Salem and Osman 2017a).

Ca versus Mg: The Ca/Mg ratio benefits from any pollution of seawater. Indication of dissolution of calcium minerals and rocks, contamination of surface water, and contact between CO_2 and $CaCO_3$ depends on the existence of high values of this ratio (Salem and Osman 2017b). Nevertheless, the operation of the base-exchange processes is strongly influenced by this ratio. 74% of water samples have Ca/Mg ratio higher than 1 (Table 6) reflecting anhydrite and gypsum dissolution. Samples with a lower-unit Ca/Mg ratio (Table 6) may be a feature of intrusion of seawater (Salem and Osman 2017b). The collected samples were usually distributed with a high correlation (r = 0.798) in the dispersed diagram (Fig. 16b, Table 5).

SO_4 versus Cl: The SO_4/Cl ratio assists in determining the dissolution effect of halite, gypsum, or anhydrite. The SO_4/Cl ratios above unity reflect the excess of sulfate than chloride and this may reflect the presence of sulfate minerals in the formation that contains water samples. All the collected water samples have SO_4/Cl ratios below unity (Table 6), reflecting the excess of chloride over sulfate which may indicate the abundance of halite in water-bearing formation deposits, seawater intrusion, and/or evaporation effect (Salem and Osman 2017b). The collected samples are scattered in the binary diagram (Fig. 16c) with a weak correlation (r = 0.414, Table 5), revealing different sources of both SO_4 and Cl.

Ca versus SO_4. Most samples collected (58%) have Ca/SO_4 ratios higher than the unit (Table 6). Ca excess in these samples indicates additional calcium by weathering minerals other than Ca-rich gypsum (Salem and Osman

2017a; Desbarats 2009; Jalali 2009). Samples with lower Ca/SO_4 ratios than 1 (42%) suggest the removal of calcium either through precipitation as calcium carbonates in and/or by ion exchange processes (Desbarats 2009; Jalali 2009; Hamzaoui-Azaza et al. 2011). The plotted samples (Fig. 16d) are scattered with moderate correlation ($r = 0.577$, Table 5).

Ca versus Cl: The Ca/Cl ratio helps to change the composition of water samples by leaching and dissolving various salts such as calcite, dolomite, gypsum, and anhydrite (Fisher and Mullican 1997; Salem and Osman 2017a and Salem et al. 2015). All the collected water samples have Ca/Cl ratios below unity (Table 6). The Ca/Cl relationship (Fig. 16e) shows a scattered pattern with high correlation coefficients (r = 0.761, Table 5). Plotted water samples are scattered mostly over the 1:2 line and this ratio confirms the seawater intrusion, especially in samples with high salinity.

HCO_3 versus ions: HCO_3 has a weak relation to Ca and Mg ($r = -0.261$, -0.112, respectively) as shown in Table 5 and Fig. 17a and b. HCO_3 is moderately related to SO_4, and weakly related to Cl^- and Na^+, where r equals 0.452, -0.112, and 0.11, respectively (Table 5 and Fig. 17c, d, and e). All the collected water samples have SO_4/HCO_3 ratios above unity but most of the collected samples (95%) have Ca/HCO_3 and Mg/HCO_3 ratios above unity (Table 6). Such low concentration of HCO_3 might be related to either calcite precipitation or reduction of carbonate minerals dissolution due to water enrichment with Ca and Mg due to silicate or/and sulfate minerals dissolution (Fisher and Mullican 1997). As shown in Fig. 18a, Ca + Mg concentration has no obvious

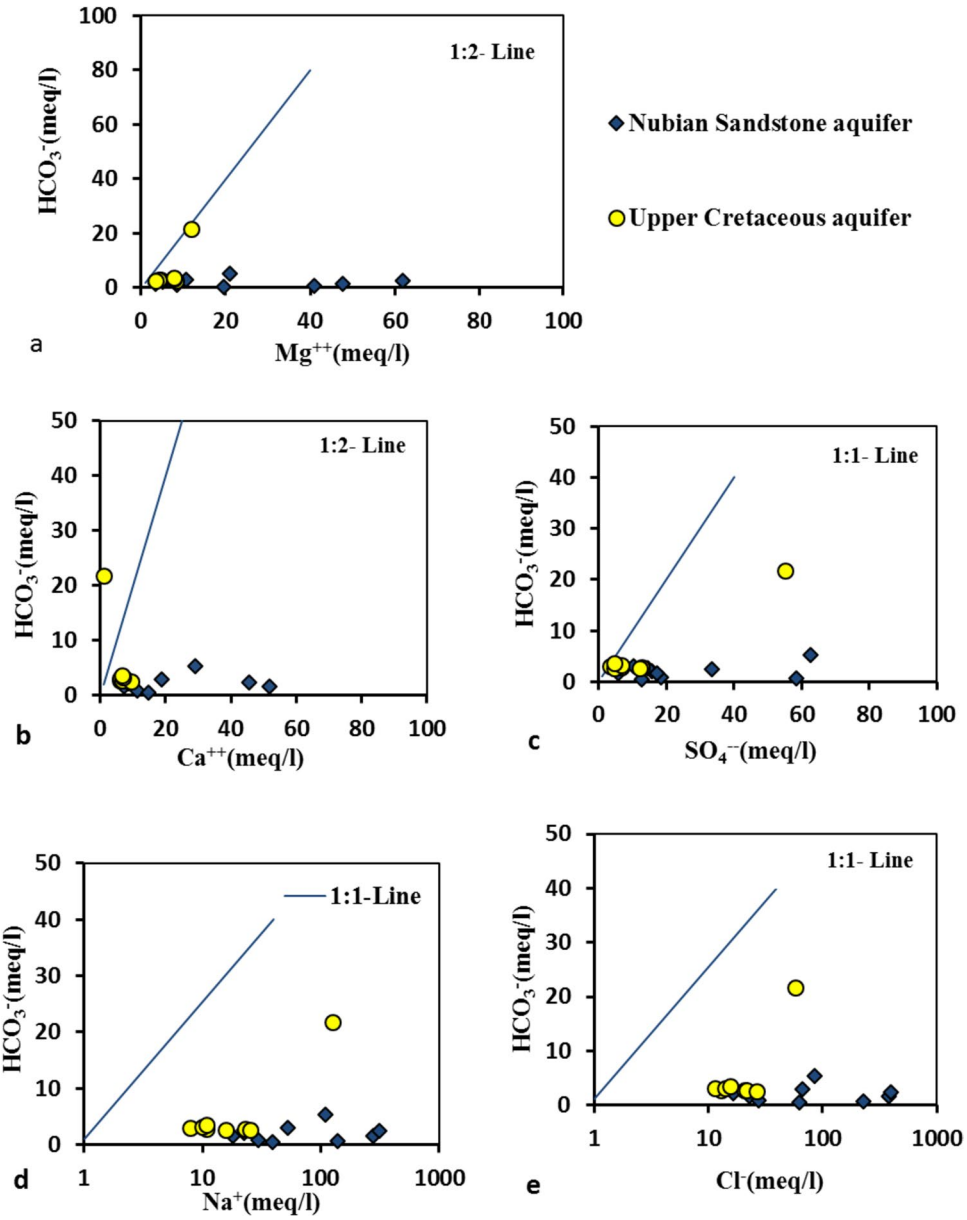

Fig. 17 Ionic relationships between HCO_3^- and other major ions

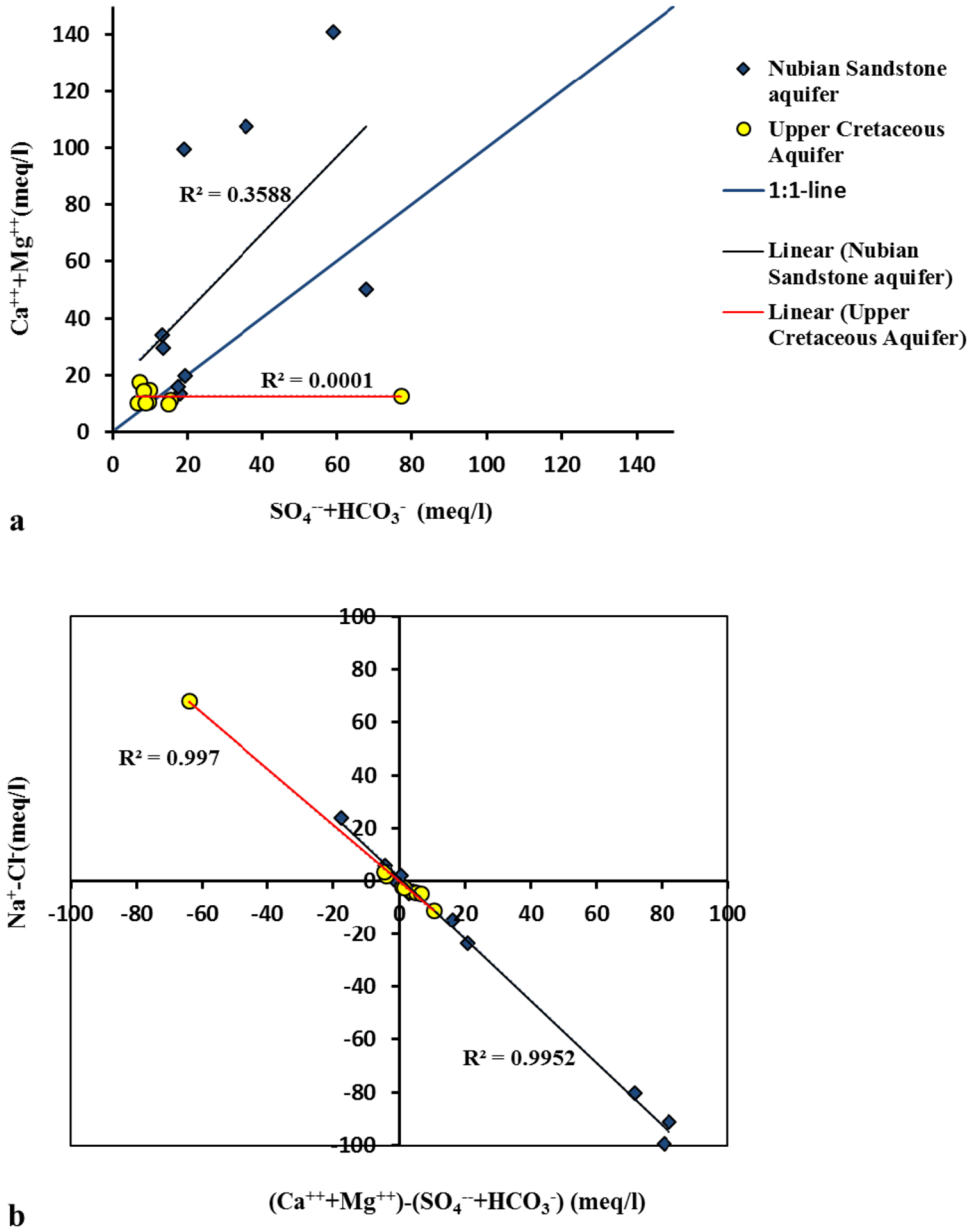

Fig. 18 Relationship between $SO_4 + HCO_3$ and $Ca + Mg$ in the dissolved sulfate and carbonate minerals **a** and a Binary diagram illustrates the ion exchange processes in the studied groundwater **b**.

relationships with $HCO_3 + SO_4$ ($r^2 = 0.3588$ and 0.0001 for the Nubian Sandstone aquifer and the Upper Cretaceous aquifer, respectively). This relationship means that Ca and Mg are not solely derived from the dissolution of gypsum, calcite, dolomite, and anhydrite, but may also be associated with weathering of silicate minerals. The ion exchange of Na and calcite and dolomite precipitations due to sulfate dissolution often extract Ca and Mg from the solution (Fisher and Mullican 1997; Salem and Osman 2017a).

Figure 18b indicates that ion exchange is occurring in the systems with a plot of $(Ca + Mg)–(SO_4 + HCO_3)$ versus Na–Cl. By subtracting Cl from Na and assuming that all the Cl comes from NaCl, groundwater samples not affected by ion exchange will plot close to zero on the y-axis. The x-axis of $(Ca + Mg)–(SO_4 + HCO_3)$ shows the amount of Ca and Mg given by congruent calcite, dolomite, and gypsum dissolution. If there are, groundwater is plotted on a straight line with a high correlation coefficient (exchange reactions in the process Jankowski et al. 1998). Data from the study area (Fig. 18b) have r^2 values of 0.9952 and 0.997 for the Nubian Sandstone aquifer and the Upper Cretaceous aquifer, respectively. From this information, it could be estimated that ion exchange reaction is a predominant process in both aquifers (Salem and Osman 2017a). To identify the relative contributions of the major weathering/dissolution mechanisms (silicate, carbonate, and evaporite) to the ion concentration in groundwater, the Na-normalized molar ratio model ($Ca/Mg/HCO_3$) suggested by Gaillardet et al. (1999) was employed

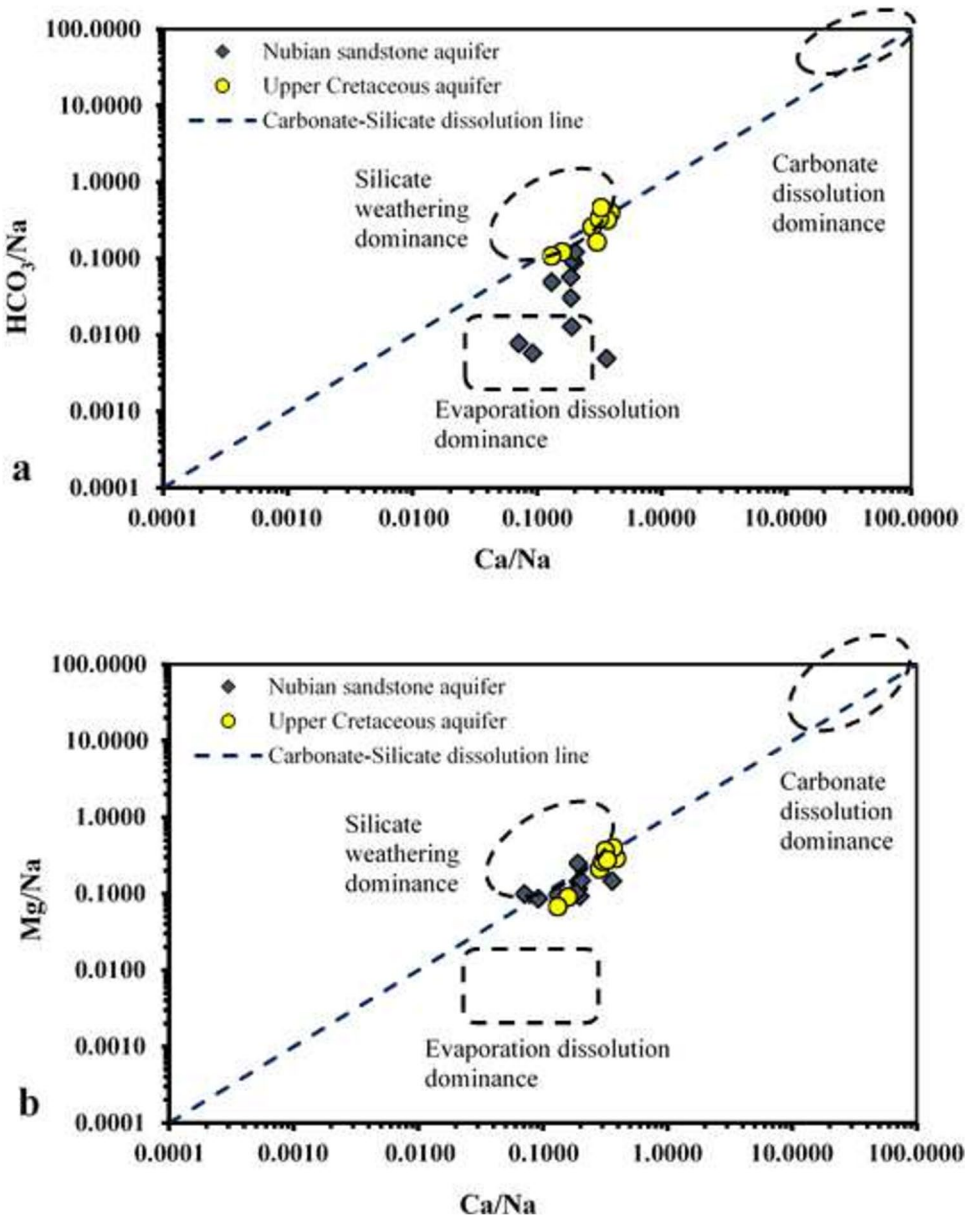

Fig. 19 Molar ratio bivariate plots of **a** Na-normalized Ca and HCO_3 and **b** Na-normalized Ca and Mg. The dashed circles represent the ranges of approximate compositions of the silicate and carbonate end members, and a dashed box represents the evaporite end member. Most groundwater samples fell in the area of silicate end member area, indicating that the majority of ions originated from silicate mineral weathering

(Fig. 19). The bivariate mixing plots (Fig. 19a and b) of Na-normalized HCO_3 versus Ca and Na-normalized Mg versus Ca showed that most of the groundwater samples of the two aquifers were within or very close to the silicate weathering domain, which indicates a significant contribution of silicate mineral weathering dissolution to the groundwater chemistry of these samples. However, some of the Nubian Sandstone groundwater samples plotted in Fig. 19b have been affected by evaporation dominance and might be seawater intrusion.

Equilibrium modeling (saturation indices)

The degree of mineral saturation in waters is determined by the percentage of saturation, defined as the saturation index (SI) = log (IAP/Ks), where IAP is the result of the ionic activity of the appropriate ions, and Ks is the product of mineral solubility. The hydrochemical program PHREEQC Interactive Program (USGS 2011) has been used to measure the distribution of species equilibrium in an aqueous solution and the saturation level of related minerals. The composition of groundwater is determined by the composition of sedimentary rocks in the basin and by hydrological characteristics such as the direction and time of residence. Table 7 and Fig. 20 show the calculated mineral saturation indices revealed that most of the collected groundwater samples are undersaturated with respect to carbonate minerals (aragonite, calcite, dolomite, and siderite), silicate minerals (albite, K-feldspar and anorthite), and chlorite, and all the obtained water samples are undersaturated for evaporates minerals (anhydrite, gypsum, halite, and sylvite) and melanterite.

Table 7 Statistical summary of the saturation indices of minerals of the collected water samples of two aquifers

Groups	Minerals/Statistics	Aquifer	Minimum	Maximum	Average	Stander deviation	Aquifer	Minimum	Maximum	Average	Stander deviation
Silicate minerals	Albite	Upper Cretaceous aquifer water samples	−1.89	1.83	−0.65	1.15	Nubian sandstone aquifer water samples	−4.47	1.15	−1.32	1.69
	Alunite		0.65	3.30	2.06	1.33		−1.16	3.70	2.50	1.75
	Anorthite		−2.53	−0.01	−1.50	1.03		−3.61	0.16	−1.88	1.44
	K-feldspar		−1.47	1.60	−0.25	0.89		−3.68	1.54	−0.97	1.63
	Quartz		−0.17	0.74	0.01	0.29		−1.35	0.74	−0.03	0.62
	Talc		−5.55	−1.06	−4.00	1.30		−8.09	1.36	−3.30	2.97
	Sepiolite		−6.58	−3.29	−5.49	0.96		−11.57	−1.69	−5.32	2.81
Clay minerals	Ca-Montmorillonite		2.50	5.88	4.20	2.47		−0.52	5.42	2.77	2.11
	Chlorite		−5.40	−2.08	−3.35	2.00		−7.22	0.95	−3.69	2.86
	Illite		1.41	5.05	3.21	2.03		−0.78	5.13	2.06	2.00
	K-mica		8.01	11.81	10.00	5.39		6.41	12.36	9.07	4.22
	Kaolinite		4.50	7.03	5.72	3.11		3.32	6.51	4.82	2.28
Carbonate minerals	Aragonite		−0.55	−0.19	−0.34	0.11		−1.05	0.23	−0.31	0.37
	Calcite		−0.40	−0.05	−0.19	0.11		−0.91	0.38	−0.16	0.37
	Dolomite		−0.72	0.35	−0.24	0.34		−1.57	0.73	−0.33	0.75
Iron oxide minerals	Goethite		6.37	7.15	6.76	2.99		5.15	9.49	7.18	3.67
	Hematite		14.75	16.31	15.53	6.86		12.30	20.98	16.36	8.26
	Jarosite-K		−3.85	−3.52	−3.69	1.63		−8.25	4.76	−1.69	3.83
	Melanterite		−6.62	−6.57	−6.60	2.91		−8.51	−4.10	−6.26	3.26
	Siderite		−0.67	−0.67	−0.67	0.30		−8.67	−0.29	−2.47	2.63
Evaporate minerals	Halite		−5.75	−3.97	−5.25	0.56		−5.16	−2.79	−4.17	0.91
	Sylvite		−7.10	−6.11	−6.76	0.32		−6.97	−3.83	−5.62	1.11
	Anhydrite		−1.81	−1.18	−1.49	0.20		−1.45	−0.07	−0.87	0.40
	Gypsum		−1.51	−0.88	−1.18	0.20		−1.15	0.23	−0.57	0.40
Gibbsite minerals			1.94	2.92	2.32	1.25		1.35	2.61	2.21	1.01

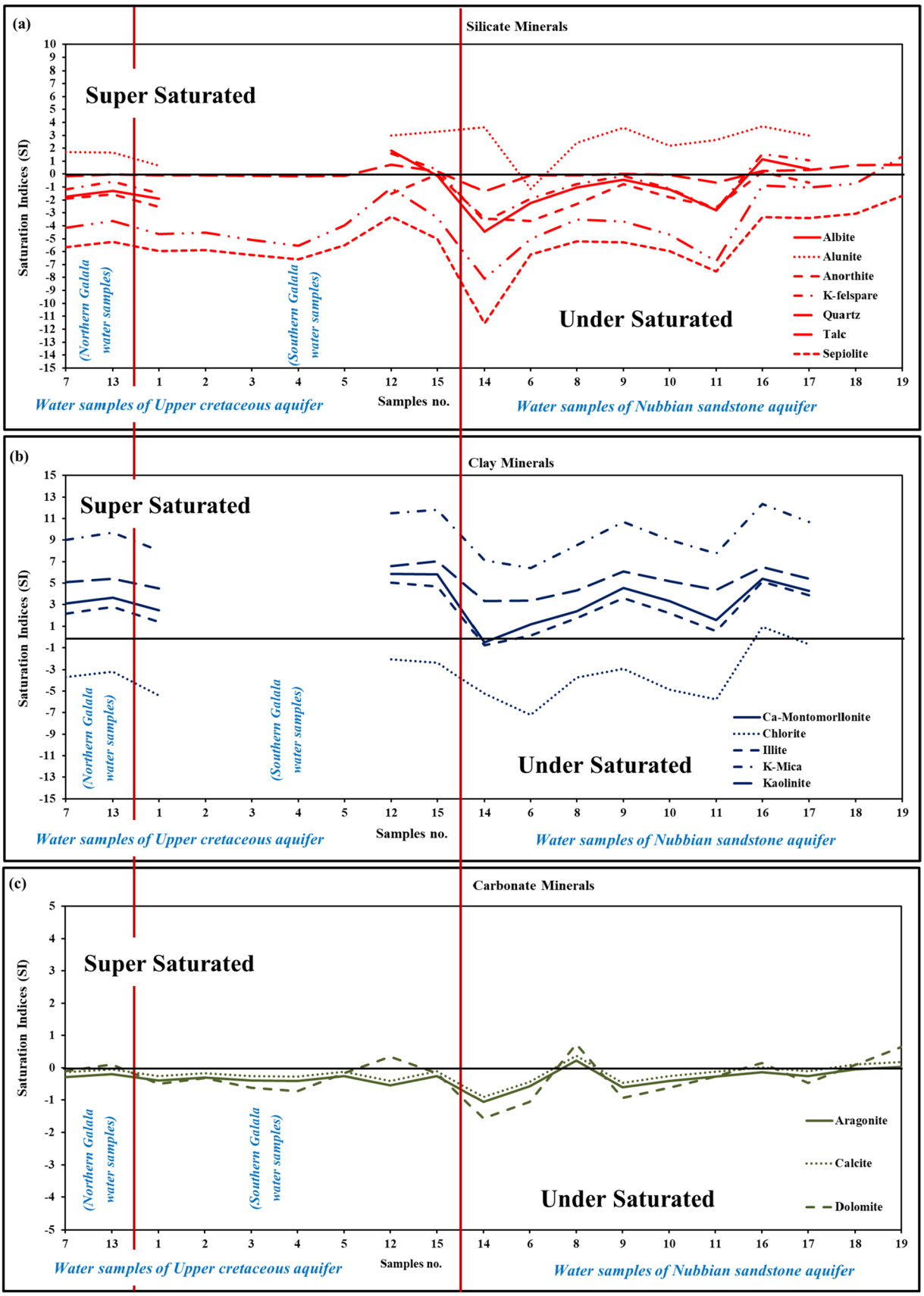

Fig. 20 Groundwater saturation indices (SI) with respect to silicate, clay, and carbonate minerals. The groundwater saturation indices (SI) with respect to iron oxide, evaporates, and Gibbsite minerals

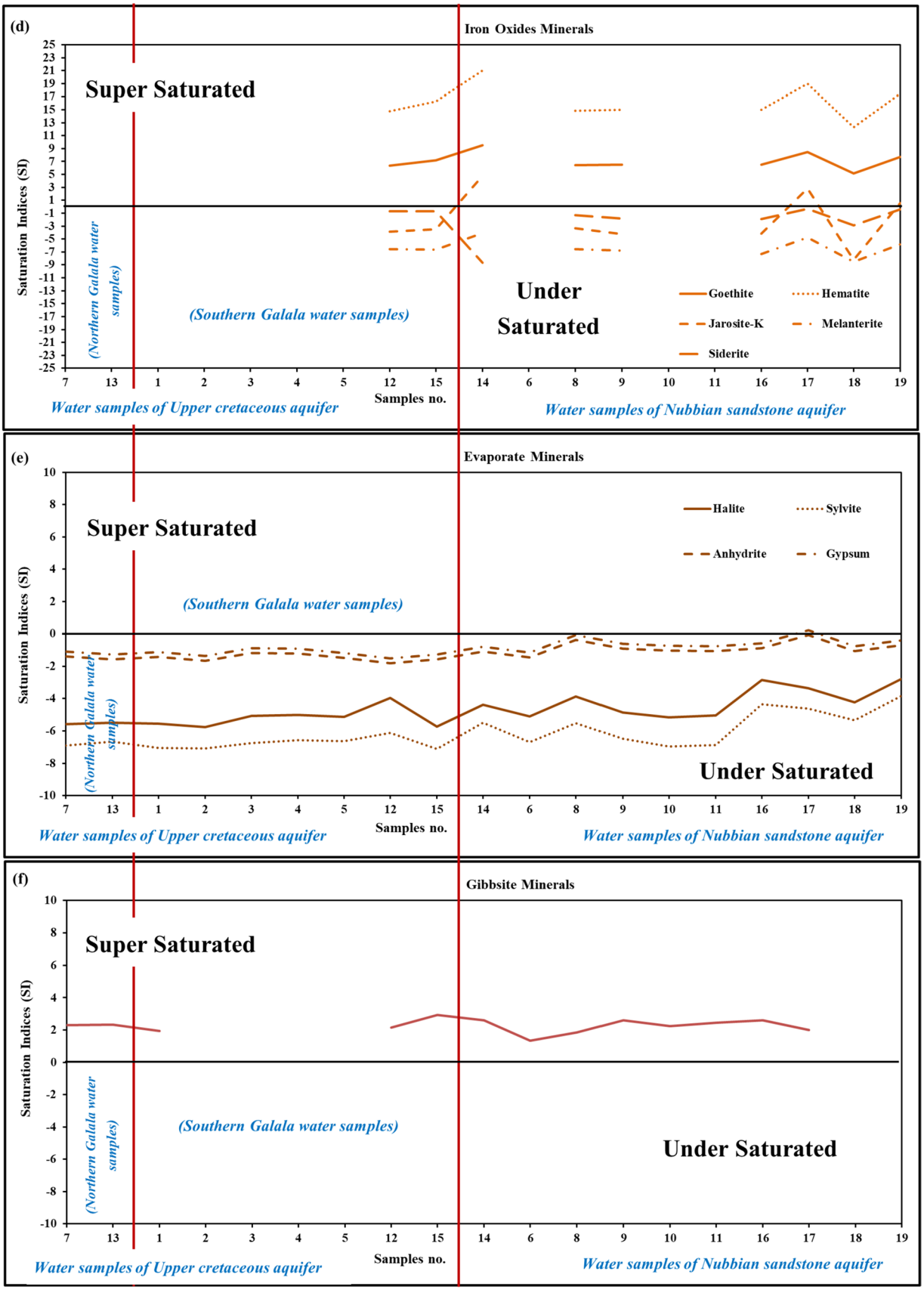

Fig. 20 (continued)

Such conditions reveal that the dissolution of these minerals along the flow system is expected. The water samples, on the other hand, were oversaturated with regard to most of the clay minerals, gibbsite and iron oxides (goethite, and hematite) and with SI close to zero for quartz. This high SI of quartz, clay, and gibbsite minerals could be due to silicate weathering. The high iron concentration could be attributed to the ferruginous mineralization in the water-bearing facies (Aly 2015). It could therefore lead to the precipitation of Fe-rich minerals (Fig. 20d).

Groundwater quality

Evaluating water in general for different uses especially irrigation and drinking is extremely important to make the most benefits of the available water or to treat it to suit a specific use (Salem et al. 2017). As for the groundwater under study, compared to WHO 2011 standards, the concentration of most elements in most samples fall below the permissible limits for drinking water, with the exception of TDS. Only sample 15 which representing the Upper Cretaceous reservoir fall below the TDS permissible limit for drinking water, and the rest of the samples are not suitable for drinking water. Therefore, desalination must be done if it is needed as drinking water.

Long-term production water management requires an understanding of irrigation water quality data. The influence and management of crops and soils are correlated with the quality of irrigation water (Salem et al. 2018, 2021b and 2022b). High-quality crops will also be produced by using high-quality irrigation water to hold other supplies at their best. The qualities of irrigation water are determined by many factors depending on the water source as APHA (2005).

An intuitive way to evaluate the overall irrigation water quality was employed in this investigation using the Irrigation Water Quality (IWQ) index (Simsek and Gunduz 2007). The IWQ index is a linear combination of several factors, including sodium ions, EC, SAR, and boron chloride. It also takes into account the toxicity of the trace element and necessitates the measurement of calcium and magnesium concentration. Since not every location may report all of these metrics, a weighted trace element average is utilized. Lastly, the index takes into account the impact of various influences on sensitive crops by combining nitrate-nitrogen, bicarbonate, and pH linearly (Simsek and Gunduz 2007). The collected water samples were subjected to a suitability analysis based on IQW according to the steps mentioned in Simsek and Gunduz, (2007). All the collected groundwater samples of the studied aquifers are plotted in the medium suitability category (Fig. 21). Despite the quality of the studied groundwater, which is beneficial for irrigation water, caution must be taken against using the water from samples 8, 12, 14, 16, 17, 18 and 19 due to its higher salinity (> 3000 mg/l) due to its proximity to the Gulf of Suez.

Conclusions

A potential contact surface between the sedimentary strata and the basement rocks at Wadi Araba area, western Gulf of Suez, Egypt can be magnetically detected. Therefore, the predicted aquifer is geometrically controlled by the basement topography. The thickness of the aquifer increases toward the east and decreases toward the west. Some magnetic contacts are observed within the sedimentary succession. The petrographic investigations suggest that the rise in magnetic anomalies and, consequently, the subsurface magnetic susceptibility contrasts, may be connected to the ferruginous properties of the aquifer deposits. Minor fractures may descend the basement and/or the sedimentary cover.

The shallow aquifers in the study area consist mainly of siliciclastic-dominated facies of Carboniferous- lower Cretaceous systems (Nubia Group) and upper Cretaceous fractured carbonate-dominated sediments. Lithostratigraphically, the exposed rocks in the studied area are represented by sandstones with thin shale and limestone bed intercalations of Carboniferous Rod El Hamal Formation, which

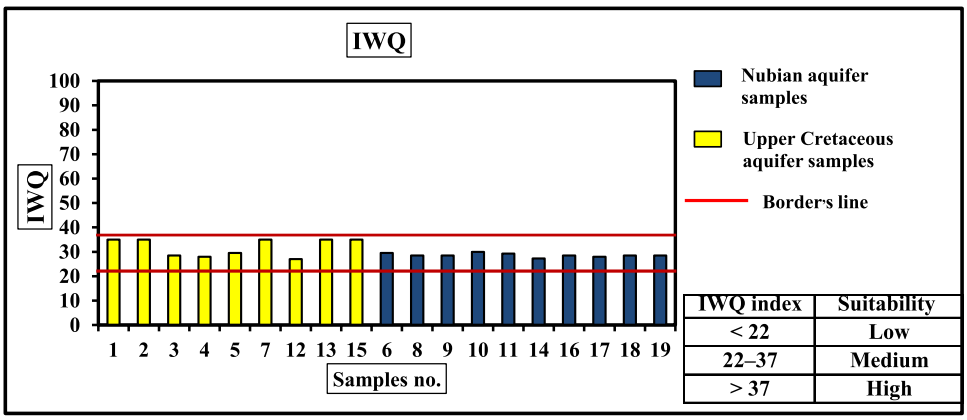

Fig. 21 Histograms show the IWQ values in the collected water samples

are unconformably overlayed by Permo-Triassic red beds of Qiseib Formation, and cross-bedded sandstones of lower Cretaceous Malha Formation. Two sides of the Wadi resemble fractured limestones of the upper Cretaceous Galala Formation.

The stratigraphical and microfacies investigations suggest that the rise in magnetic anomalies and, consequently, the subsurface magnetic susceptibilities may be connected to the ferruginous properties of the Nubian Sandstone aquifer. A potential contact surface between the sedimentary strata and the basement rocks can be magnetically detected. Therefore, the predicted aquifer is geometrically controlled by the basement topography. The thickness of the aquifer increases toward the east and decreases toward the west. No major magnetic contacts are observed with the sedimentary succession. Minor fractures may descend the basement and/or the sedimentary cover.

Quartz arenite, subarkose, sublitharenite, and greywacke are the main constituents microfacies of the siliciclastic sediments, whereas mudstone/wackestone, packstone/Grainstone resemble the carbonate rocks of the shallow aquifers. The main diagenetic processes that have affected the studied shallow aquifer rocks include mechanical and chemical compaction, the precipitation of calcite, dolomite, and silica (in the form of quartz overgrowths), as well as the dissolution of unstable minerals and shell fragments. These minerals result from the chemical interaction between rocks and groundwater of the studied aquifer. However, some of the diagenetic processes reduced the primary porosity of the aquifers, e.g., compaction, cementation, and recrystallization, while others led to the formation of secondary porosity and changed the groundwater chemistry as dissolution and fracturing.

The groundwater samples under investigation are categorized as hard brackish and very hard saline based on total dissolved solids (TDS) and total hardness (TH). Statistically, the collected samples are classified into five groups (A, B, C, D, and E). All groups exhibit NaCl-type water, except for group B, which has Na-SO_4 type water. Higher TDS values are associated with the Nubian Sandstone aquifer in groups A, B, and C (with average values of 20,766, 9143, and 4431 mg/l, respectively). Conversely, lower TDS values are observed in the D and E groups (with average values of 1209 and 2210 mg/l, respectively), which are primarily sourced from fractured limestone springs. Elevated TDS, Si, Al, Fe, and Mg concentration may be indicative of seawater intrusion and/or water–rock interaction in the Nubian sandstone aquifer, while lower salinity values in fractured limestone samples may result from direct recharge from rainwater. According to the Piper diagram, most samples exhibit NaCl type, signifying primary salinity, with some samples categorized as $CaMgSO_4$ type.

The dendrograms illustrate two distinct ion associations in Nubian Sandstone groundwater: SO4–Ca–Mg–CO_3–K–Si–CO_3 and Cl–Na, suggesting water–rock interaction and seawater intrusion, respectively. In contrast, the Upper Cretaceous aquifer displays two different ion associations: Na–Cl–SO_4 and Ca-Mg-HCO_3-K-Si-CO_3. The Na-SO_4 association indicates ion exchange between Na from rocks and Ca from dissolved gypsum, while the presence of K–HCO_3–Ca–Mg points to a freshwater source. Pearson's correlation analysis suggests that Ca, Mg, Na, K, Cl, and Si are the primary components influencing groundwater salinity.

The relationships among total dissolved solids (TDS), ionic ratios, and other associations imply that seawater intrusion, ion exchange, and silicate weathering are the predominant hydrogeochemical processes affecting the examined groundwater. Samples with low carbonate concentration may be linked to an excess of dissolved calcium resulting from silicate weathering and/or gypsum dissolution. Mineral saturation indices indicate that most collected groundwater samples are undersaturated with carbonate minerals (aragonite, calcite, dolomite, and siderite) and silicate minerals (albite, feldspar, and anorthite), as well as chlorite. Additionally, all samples show insufficient saturation with evaporite minerals (anhydrite, gypsum, halite, and sylvite) and melanterite.

Conversely, water samples are supersaturated with respect to most clay minerals, gypsite, and iron oxides (goethite and hematite), with a saturation index close to zero for quartz. The elevated saturation indices for quartz, clay, and gibbsite minerals may be attributed to silicate weathering. The higher iron concentration is likely linked to ferrous mineralization in the water-bearing facies, potentially leading to the precipitation of iron-rich minerals. Studied groundwater is unsuitable for drinking except one sample, while it is moderately suitable for irrigation with caution for higher salinity in samples located near to the Gulf of Suez.

Acknowledgements The work was funded by the National Research Institute of Astronomy and Geophysics (NRIAG).

Funding Open access funding provided by The Science, Technology & Innovation Funding Authority (STDF) in cooperation with The Egyptian Knowledge Bank (EKB).

Data availability The data were collected and analyzed primarily by us.

Declarations

Conflict of interest The authors have no conflicts of interest to declare that are relevant to the content of this article.

Consent to participate The authors consent to participate in this research study.

References

Abdallah AM, El Adindani A (1963) Stratigraphy of Upper Paleozoic rocks, western side of Gulf of Suez. Geol Surv Egypt 25:18p

Abdallah AM, El Adindani A, Fahmy N (1965) Stratigraphy of the Lower Mesozoic Rocks, Western side of the Gulf of Suez, Egypt. Egypt Geological Survey and Mineral Research Department Paper No. 27, Cairo, Egypt

Abdelazeem M, Fathy MS, Khalifa MM (2019) Integrating magnetic and stratigraphic data to delineate the subsurface features in and around new Galala City, Northern Galala Plateau. Egypt NRIAG J Astron Geophys 8(1):131–143

Abdelazeem M, Salem ZE, Fathy MS, Saleh M (2020) Impact of lithofacies and structures on the hydrogeochemistry of the lower miocene aquifer at Moghra Oasis, North Western Desert Egypt. Nat Resour Res 29(6):3789–3817. https://doi.org/10.1007/s11053-020-09679-3

Abdelazeem M, Fathy MS, Gobashy M (2021) Magnetometric identification of sub-basins for hydrocarbon potentialities in Qattara Ridge, North Western Desert Egypt. Pure Appl Geophys 178:995–1020. https://doi.org/10.1007/s00024-021-02678-2

Abdelrahman EM, Abdelazeem M, Gobashy M (2019) A minimization approach to depth and shape determination of mineralized zones from potential field data using the Nelder–Mead simplex algorithm. Ore Geol Rev 114:103–123

Aggour TA (1990) Response of geomorphological and geological features on groundwater in Wadi Araba, Eastern Desert, Egypt. M.Sc. Thesis Fac. Sci. Ain Shams Univ. p 179

Al Garni MA, Gobashy MM (2010) Ground magnetic Investigation of subsurface structures affecting Wadi Thuwal area, KSA. J King Abdulaziz Univ, JKAU: Earth Sci 21(2):167–193

Al Garni MA, Hassanein H, Gobashy M (2006) Geophysical Investigation of groundwater in Wadi Lusab, Haddat ash Sham area, Makkah Al-Mukarramah. Arab Gulf J Sci Res 24(2):83–93

Al Garni MA, El-Behiry MG, Gobashy M (2012) Geophysical survey for geological hazards assessment of Wadi Thuwal area, KSA: a case history. Arab J Geosci 5:133–146. https://doi.org/10.1007/s12517-010-0147-9

Aly AA (2015) Hydrochemical characteristics of Egypt western desert oases groundwater. Arab J Geosci 8(9):7551–7564

APHA (2005) WEF, 2005. Standard methods for the examination of water and wastewater, 21, 258-259

Araffa SAS, Gobashy MM, Khalil MH, Abdelaal A (2021) Integration of geophysical techniques to detect geotechnical hazards: a case study in Mokattam, Cairo, Egypt. Bull Eng Geol Environ 80:8021–8041. https://doi.org/10.1007/s10064-021-02388-y

Ashour MA, El Attar ST, Rafaat YM, Mohamed MN (2009) Water resources management in Egypt. J Eng Sci 37(2):269–279

Azeem MA, Mekkawi M, Gobashy MM (2014) Subsurface structures using a new integrated geophysical analysis, South Aswan, Egypt. Arab J Geosci 7(12):5141–5157. https://doi.org/10.1007/s12517-013-1140-x

Bandel K, Kuss J (1987) Depositional environment of the pre-rift sediments: Galala Heights (Gulf of Suez, Egypt). Berliner Geowiss Abh A 78:1–48

Banerjee P, Prasad B (2020) Determination of concentration of total sodium and potassium in surface and ground water using a flame photometer. Appl Water Sci 10(5):1–7

Bjorkum PA, Walderhaug O, Aase NE (1993) A model for effect of illitization on porosity and quartz cementation of sandstones. J Sediment Petrol 63(6):1089–1091

Conoco (1987) Geological map of Egypt 1:500,000. The Egyptian General Petroleum Corporation, Cairo

Constable SC, Parker RL, Constable CG (1987) Occams' inversion: a practical algorithm for generating smooth models from electromagnetic sounding data. Geophysics 52(3):289–300

De Smet TS, Nikulin A, Romanzo N, Graber N, Dietrich C, Puliaiev A (2020) Successful application of drone-based aeromagnetic surveys to locate legacy oil and gas wells in Cattaraugus County New York. J Appl Geophys 186:104250. https://doi.org/10.1016/j.jappgeo.2020.104250

Desbarats AJ (2009) On elevated fluoride and boron concentrations in groundwaters associated with the Lake Saint-Martin impact structure. Manitoba Appl Geochem 24(5):915–927

Deshpande SM, Aher KR (2012) Evaluation of groundwater quality and its suitability for drinking and agriculture use in parts of Vaijapur, District Aurangabad, MS, India. Res J Chem Sci ISSN 2231:606X

Dobrin MB, Savit CH (1988) Introduction to geophysical prospecting. McGraw-Hill Book Co, Singapore

Dunham RJ (1962) Classification of carbonate rocks according to depositional texture - A symposium in classification of carbonate rocks. AAPG Mem 1:108–121

Dyke L (1999) Regional groundwater and stream chemistry survey, Oak Ridges Moraine, Ontario. In: Current Research 1999-E, Geol. Surv. Canada, pp 111–121.

Ehrenberg SN (1990) Relationship between diagenesis and reservoir quality in sandstones of the Garn Formation, Haltenbanken, mid-Norwegian continental shelf. Am Asso Petrol Geol Bull 74:1538–1558

El-Aziz SHA (2017) Evaluation of groundwater quality for drinking and irrigation purposes in the north-western area of Libya (Aligeelat). Environ Earth Sci 76(4):147

El-Sawy EK, Eldougdoug A, Gobashy M (2018) Geological and geophysical investigations to delineate the subsurface extension and the geological setting of Al Ji`lani layered intrusion and its mineralization potentiality, Ad Dawadimi District, Kingdom of Saudi Arabia. Arab J Geosci 11:32. https://doi.org/10.1007/s12517-017-3368-3

Ezzeldin H (2010) "Hydrogeochemical Studies on the Area Between El-Ain El-Sukhna and Wadi Araba, Gulf of Suez, Egypt". Ph.D. Thesis Fac. Sci. Benha Univ. p 142

Fergany E, Mekkawi M, Abdel Azeem M, Khalil A (2014) Integrated geologic and geophysical studies of north unstable shelf seismicity, Egypt. Arab J Geosci. https://doi.org/10.1007/s12517-014-1620-7

Fisher RS, Mullican WF (1997) Hydrochemical evolution of sodium-sulfate and sodium-chloride groundwater beneath the northern Chihuahuan Desert, Trans-Pecos, Texas, USA. Hydrogeol J 5(2):4–16

Folk RL (1962) Spectral subdivision of limestone types. - A symposium in classification of carbonate rocks. AAPG Mem 1:62–84

Gaillardet J, Dupré B, Louvat P, Allègre CJ (1999) Global silicate weathering and CO2 consumption rates deduced from the chemistry of large rivers. Chem Geol 159(1–4):3–30

Garrels RM (1976) A survey of low temperature water mineral relations. In: Interpretation of environmental isotope and hydrogeochemical data in groundwater hydrology: Vienna, International Atomic Energy Agency, pp 65–84.

Gobashy MM, Al-Garni MA (2008) High resolution ground magnetic survey (HRGM) for determining the optimum location of

Subsurface Dam in Wadi Nu`man, Makkah Al Mukarammah, KSA. J King Abdulaziz University Earth Sci 19:57–83
Gobashy M, Eldougdoug A, Abdelazeem M, Abdelhalim A (2021a) Future development of gold mineralization utilizing integrated geology and aeromagnetic techniques: a case study in the Barramiya Mining District, Central Eastern Desert of Egypt. Nat Resour Res 30:2007–2028. https://doi.org/10.1007/s11053-021-09824-6
Gobashy MM, Metwally AM, Abdelazeem M, Soliman KS, Abdelhalim A (2021b) Geophysical exploration of shallow groundwater aquifers in arid regions: a case study of Siwa Oasis, Egypt. Nat Resour Res 30(5):3355–3384
Gobashy MM, Abbas EAS, Soliman KS et al (2022) Mapping of gold mineralization using an integrated interpretation of geological and geophysical data—a case study from West aranes, South Eastern Desert, Egypt. Arab J Geosci 15:1692. https://doi.org/10.1007/s12517-022-10955-0
Gomaa MA, Aggour TA (1999) Hydrogrological and hydrogeochemical conditions of carbonate aquifers in the Gulf of Suez region, Egypt. Bull Fac Sci Assiut Univ, pp 191–214
Graton LC, Fraser HJ (1935) Systematic packing of spheres, with particular relation to porosity and permeability. J Geol 43:785–909
Hamzaoui-Azaza F, Ketata M, Bouhlila R, Gueddari M, Riberio L (2011) Hydrogeochemical characteristics and assessment of drinking water quality in Zeuss–Koutine aquifer, southeastern Tunisia. Environ Monit Assess 174(1–4):283–298
Hasan SS, Salem ZE, Sefelnasr A (2023) Assessment of hydrogeochemical characteristics and seawater intrusion in coastal aquifers by integrating statistical and graphical techniques: quaternary Aquifer, West Nile Delta, Egypt. Water 15(10):1803. https://doi.org/10.3390/w15101803
Hach (1990) Chemical procedure explain. Hach Technical Center for Applied Analytical Chemistry, Instrument catalogue, Colorado, 4B
Hoaghia M-A, Moldovan A, Kovacs E, Mirea IC, Kenesz M, Brad T, Cadar O, Micle V, Levei EA, Moldovan OT (2021) Water quality and hydrogeochemical characteristics of some karst water sources in Apuseni Mountains. Romania Water 13(6):857. https://doi.org/10.1016/j.scitotenv.2017.07.176
Ibrahim RG, Lyons WB (2017) Assessment of the hydrogeochemical processes affecting groundwater quality in the Eocene limestone aquifer at the desert fringes of El Minia Governorate, Egypt. Aquatic Geochem 23(1):33–52
Jalali M (2009) Geochemistry characterization of groundwater in an agricultural area of Razan, Hamadan. Iran. Environ Geol 56(7):1479–1488
Jankowski J, Acworth RI, Shekarforoush S (1998) Reverse ion-exchange in deeply weathered porphyritic dacite fractured aquifer system, Yass, New South Wales, Australia. In: Arehart GB, Hulston JR (eds.) Proceedings of 9th international symposium on water–rock interaction. Balkema, Rotterdam, pp 243–246
Khan MMA, Umar R (2010) Significance of silica analysis in groundwater in parts of central ganga plain, Uttar Pradesh, India. Curr Sci 98(9):1237–1240
Kora M, Mansour Y (1992) Stratigraphy of some Permo- Carboniferous successions in the northern Galala, Gulf of Suez region, Egypt. N Jb Geol Paläont Abh 185:377–394
Kora M, Khalil H, Sobhy M (2001) Stratigraphy and microfacies of some Cenomanian-Turonian successions in the Gulf of Suez region, Egypt. Egypt J Geol 45(1):413–439
Kora M (1998) The Permo-Carboniferous outcrops of the Gulf of Suez region, Egypt: stratigraphic classification and correlation. In: Crasquin-Soleau S, Izar! A, Vaslet O. & De Wever P. (eds.), Peri-Tethys: stratigraphic correlations 2, *Geodiversitas* 20(4): 701–721.
Kumar G (2005) Geology of Uttar Pradesh and Uttaranchal. Geological Society of India, Bangalore, pp 267–291
Kumar M, Kumari K, Singh UK, Ramanathan AL (2009) Hydrogeochemical processes in the groundwater environment of Muktsar, Punjab: conventional graphical and multivariate statistical approach. Environ Geol 57(4):873–884
Lee JY, Song SH (2007) Evaluation of groundwater quality in coastal areas: implications for sustainable agriculture. Environ Geol 52(7):1231–1242
Moustafa AR, Khalil MH (1994) Rejuvenation of the eastern Mediterranean-passive continental margin in northern and central Sinai: new data from the themed Fault. Geol Mag 131(4):435–448
Nabawy BS, Khalil HM, Fathy MS, Ali F (2020) Impacts of microfacies type on reservoir quality and pore fabric anisotropy of the Nubia sandstone in the central Eastern Desert. Egypt- Geol J 55:4507–4524
Nazih M, Gobashy MM, Salem Z, Soliman KS, Hassan AA (2022) Hydrogeochemical and geophysical investigations to delineate underground water aquifer in arid regions: a case study, Gara oasis, Egypt. Contrib Geophys Geodesy 52(3):307–357. https://doi.org/10.31577/congeo.2022.52.3.1
Pettijohn FJ, Potter E, Siever R (1987) Sand and Sandstone. Springer Verlag, Berlin, pp 1–553
Rajendra Prasad D, Sadashivaiah C, Rangnna G (2009) Hydrochemical characteristics and evaluation of groundwater quality of Tumkur Amanikere Lake Watershed, Karnataka, India. J Chem 6(S1):S211–S218
Rehman F, Abdelazeem M, Gobashy MM, Harbi HM, Rehman S (2019) Application of magnetic method to define the structural setting controlling the contaminated area of Wadi Bani Malik, East Jeddah, Saudi Arabia. Bollettino Di Geofisica Teorica Ed Applicata 60(1):97–122. https://doi.org/10.4430/bgta0269
Reid AB, Allsop JM, Granser H, Millett AJ, Somerton IW (1990) Magnetic interpretation in three dimensions using Euler deconvolution. Geophysics 55(1):80–91. https://doi.org/10.1190/1.1442774
Salem ZE, El-Horiny MM (2014) Hydrogeochemical evaluation of calcareous eolianite aquifer with saline soil in a semiarid area. Environ Sci Pollut Res. https://doi.org/10.1007/s11356-014-2735-9
Salem ZES, Osman OM (2017a) Use of major ions to evaluate the hydrogeochemistry of groundwater influenced by reclamation and seawater intrusion, West Nile Delta, Egypt. Environ Sci Pollut Res 24(4):3675–3704
Salem ZE, Atwia MG, El-Horiny MM (2015) Hydrogeochemical analysis and evaluation of groundwater in the reclaimed small basin of Abu Mina, Egypt. Hydrogeol J 23(8):1781–1797
Salem ZE, Abdelrahman K, Kováčiková S, Badran OM (2021b) Use of various statistical techniques to assess the vertical and lateral change in the groundwater chemistry of Quaternary aquifer in an irrigated highly populated area. J King Saud Univ-Sci 33:1015562. https://doi.org/10.1016/j.jksus.2021.101556
Salem ZE, ElNahrawy A, Attiah AM, Edokpayi JN (2022a) Vertical and spatial evaluation of the groundwater chemistry in the Central Nile Delta Quaternary aquifer to assess the effects of human activities and seawater intrusion. Front Environ Sci 10:961059. https://doi.org/10.3389/fenvs.2022.961059
Salem ZE, Osman OM (2017b) Use of geoelectrical resistivity to delineate the seawater intrusion in the northwestern part of the Nile Delta, Egypt. In: The Handbook of Environmental Chemistry (Groundwater in the Nile Delta, 2019). Springer, Berlin, Heidelberg
Salem ZE, Elsaiedy G, ElNahrawy A (2017c) Assessment of the groundwater quality for drinking and irrigation purposes in the central Nile Delta Region, Egypt. In: The Handbook of Environmental Chemistry (Groundwater in the Nile Delta, 2019). Springer, Berlin, Heidelberg

Salem ZE, Al Temamy AM, Salah MK, Kassab M (2018) Evaluation of water resources qualities for agriculture irrigation in abu Madi area, northern Middle Nile Delta. In: The Handbook of Environmental Chemistry (Conventional Water Resources and Agricultural in Egypt, 2019). Springer, Berlin, Heidelberg. ISBN 978-3-319-95065-5

Salem ZE, Fathy MS, Helal AI, Afifi SY, Attiah AM (2021b). Groundwater quality for irrigation as an of Sustainable Development Approaches: a case study of semi-arid area around Ismailia Canal, Eastern Nile Delta, Egypt In A. Negm and A. Elkhouly (eds.), Groundwater in Egypt's Deserts, Springer Water, https://doi.org/10.1007/978-3-030-77622-0_12

Salem ZE, Sefelnasr A, Hasan SS (2022b) As a water resources management tool, groundwater quality assessment for irrigation in the Young Alluvial Plain of Western Nile Delta, Egypt, In: A. M. Negm and M. El-Rawy (eds.), Sustainability of Groundwater in the Nile Valley, Egypt, Earth and Environmental Sciences Library, https://doi.org/10.1007/978-3-031-12676-5_8

Scheibner C, Marzouk AM, Kuss J (2001) Maastrichtian-Early Eocene litho-biostratigraphy and palægeography of the northern Gulf of Suez region, Egypt. J Afr Earth Sci 32(2):223–255

Schweinfurth G (1885) Sur la découverte d'une fauna Paléozoique dans le Grès d'Egypte. Bull Inst Egypt 6(2):239–255

Selly RC (1998) Elements of Petroleum Geology, 2nd edn. Academic Press Limited, California, pp 1–470

Simsek C, Gunduz O (2007) IWQ Index: a GIS-integrated technique to assess irrigation water quality. Environ Monit Assess 128:277–300. https://doi.org/10.1007/s10661-006-9312-8

Thompson DT (1982) EUlDPH: A new technique for making computer-assisted depth estimates from magnetic data. Geophysics 47:31–37

USGS (2000) Is Seawater Intrusion Affecting Ground Water on Lopez Island, Washington? Has Seawater Intruded Into Lopez Island'S the Source of Lopez What Is Seawater. USGS Fact Sheet 057-00. http://pubs.usgs.gov/fs/2000/fs-057-00/pdf/fs05700.pdf

USGS (2011) A graphical user interface to the geochemical model PHREEQC Interactive Computer Program of USGS 2.18

Wang S, Zheng W, Currell M, Yang Y, Zhao H, Lv M (2017) Relationship between land-use and sources and fate of nitrate in groundwater in a typical recharge area of the North China Plain. Sci Total Environ 609(607):20

Younis A, Osman OM, Khalil AE, Nawawi M, Soliman M, Tarabees EA (2019) Assessment groundwater occurrences using VES/TEM techniques at North Galala plateau, NW Gulf of Suez, Egypt. J Afr Earth Sci 160:103613